DESIGN AND FUSED FILAMENT FABRICATION OF MULTILAYERED MICROCHANNELS FOR SUBWAVELENGTH AND BROADBAND SOUND ABSORPTION

Josué Costa-Baptista[1,2,3], Edith Roland Fotsing[1,3*], Jacky Mardjano[4], Daniel Therriault[2,3] and Annie Ross[1,3]

1) Laboratory for Acoustics and Vibration Analysis (LAVA), Department of Mechanical Engineering, École Polytechnique de Montréal, P.O. Box 6079, Station Centre-Ville, Montréal (Québec) Canada, H3C 3A7
2) Laboratory for Multiscale Mechanics (LM2), Department of Mechanical Engineering, École Polytechnique de Montréal, P.O. Box 6079, Station Centre-Ville, Montréal (Québec) Canada, H3C 3A7
3) Research Center for High Performance Polymer and Composite Systems (CREPEC), Department of Mechanical Engineering, McGill University, 817 rue Sherbrooke Ouest, R.270, Montréal (Québec) Canada, H3A 0C3
4) Safran Aircraft Engines, Villaroche, Rond Point René Ravaud - Réau, 77550 Moisy-Cramayel Cedex, France

Corresponding author e-mail: e-r.fotsing@polymtl.ca*

Highlights

- Numerical modelling and optimization of multilayered microchannels lead to broadband and subwavelength absorption at three frequency ranges (500-2400Hz, 2400-6500Hz and 500-6500Hz);
- Innovative FFF manufacturing technique allows one-step production of microchannels with 100µm and optimized multilayered structures with 30-layers (air volume > 80%);
- 30 mm-thick multilayered microchannels present sound absorption average up to 0.87 and noise reduction coefficient (NRC) up to 0.49;
- PLA 3D printed multilayered microchannels exhibit a compressive modulus up to 468MPa and compressive yield strength up to 9MPa.

Graphical abstract

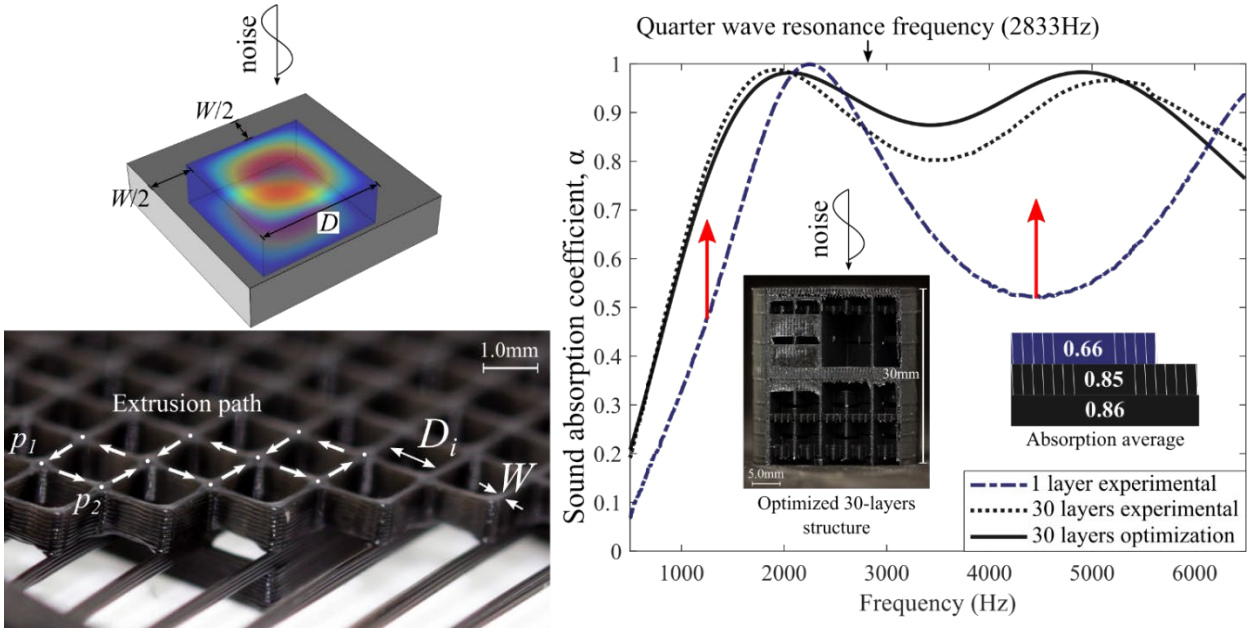

Abstract

A comprehensive procedure to design and manufacture multilayered microchannels presenting competitive mechanical properties, effective subwavelength and near perfect broadband sound absorption in targeted frequency ranges is presented. The acoustic properties of microchannels are predicted with the Johnson-Champoux-Allard-Lafarge (JCAL) model. The JCAL parameters are calculated with the Two-scale Asymptotic Method (TAM) and the sound absorption coefficient of multilayered microchannels is simulated with the transfer matrix method (TMM). The simplex Nelder-Mead optimization method is used to find the size of the channels and the stacking sequence leading to effective acoustic absorption for three different frequency ranges (500-2400Hz, 2400-6500Hz and 500-6500Hz). 30 mm-thick samples with up to 30-layers of unobstructed and non interconnected channels and microchannels were successfully produced via fused filament fabrication (FFF). The minimum channels size is ~100µm which is very appropriate to produce micro-perforated panels or acoustic liners with optimal absorption and different degrees of freedom. Multilayered microchannels with absorption average up to 0.87 and noise reduction coefficient (NRC) up to 0.49 were produced. The multilayered microchannels offer a good compromise between effective acoustic properties and useful mechanical properties compared to other 3D printed acoustic structures and can be considered as viable candidates for applications where structural resistance is required.

Keywords: acoustic modelling, sound absorbing materials, design and optimization, additive manufacturing, multifunctional structures

1. Introduction

The interest on periodic porous structures (PPS) has grown recently now that promising additive manufacturing (AM) methods allow the creation of sound absorbing materials with well-defined geometrical parameters (e.g., pore size and wall width) [1]. PPS are potential replacements for traditional stochastic foams for sound absorption owing to their design flexibility combined to their lightweight and broadband sound absorption capabilities. Several acoustic concepts can be found in the literature, for instance, uniform micro-lattices [1–3], sonic crystals [4], tubes and micro-tubes [5–7], fibrous sound absorbers [8], micro-helix metamaterials [9] and other cellular structures [10]. Other complex microstructures such as triply periodic minimal surfaces (TPMS) [11], uniform Kelvin cells [12], structures made by the subtraction of spheres from cubic cells (SSCC) [13] and interlinked networks of resonant chambers (INRC) [14,15] were made via different AM techniques. Among these, only few researches focus on developing a comprehensive approach to optimize the microstructure of the proposed material. Therefore, the maximum capacity of most PPS for sound absorption applications still undetermined.

In general, the absorption spectrum of 3D printed uniform PPS with arbitrary or optimized pore sizes is composed of ripples with higher absorption at the so-called quarter-wave resonance frequency and harmonics (QWRF $\cong c/4T$, where c is the wave propagation speed in air and T is the structure's thickness). Little absorption can be achieved at subwavelength frequencies unless thick structures is used which is prohibitive in many practical applications. Double porosity [16–18], multilayered structures [19,20] and resonant inclusions [21–23] are considered efficient ways to increase the subwavelength absorption of traditional porous structures. Concerning 3D-printed periodic structures, subwavelength absorption was achieved with uniform and multilayer perforated panels (MPP) [24–26]. The pore diameter obtained varies from 0.9 to 3.0mm. However, according to Maa's theory [27] supported by [28], MPP show optimal subwavelength absorption when the panels contain micro-perforations (from 25 to 300μm diameter). Moreover, the perforation ratio can be tuned to achieve impedance matching and perfect sound absorption (i.e., $\alpha = 1$ when the real and imaginary parts of the impedance of the MPP surrounded by air are 1 and 0, respectively [29]). Boulvert *et al.* [30] presented the simulation and experimental validation of subwavelength sound absorption of acoustic micro-lattices with optimally graded geometrical parameters. More recently, numerical simulations led to the design of optimally graded SSCC and multilayered microchannels presenting concomitant subwavelength and broadband sound absorption [31,32]. Only gradients with monotonic variation of pore size in the wave propagation direction are considered in works dealing with SSCC and micro-lattices which restricts the solution space

for the optimization procedure. In addition, only few information on the mechanical properties of sound absorbing PPS is available in the literature which limits its potential for practical applications [33].

In this work a comprehensive approach including a numerical optimization procedure and an accurate and repeatable FFF manufacturing method are developed to design and fabricate polymeric multilayered microchannels leading to simultaneous subwavelength and broadband sound absorption. Multilayered microchannels are numerically optimized to provide the best sound absorption for three frequency ranges: 500-2400Hz, 2400-6500Hz and 500-6500Hz. Besides, a design rule to avoid microchannels obstruction is applied, and no restrictions on the pore size distribution of the accepted solutions are imposed. The acoustic properties of each layer are predicted with the Johnson-Champoux-Allard-Lafarge (JCAL) model. The JCAL parameters of structures with channels size varying from 50µm to 15mm are calculated using the Two-scale Asymptotic Method (TAM) solved with the Finite Element Method (FEM). The sound absorption coefficient of multilayered microchannels is simulated with the transfer matrix method (TMM). 30mm-thick cylindrical samples (30mm diameter) of effective multilayered microchannels are successfully produced and their acoustic absorption are measured using an impedance tube. Simulated and experimental sound absorption are compared. To complete the analysis, compression tests are carried out to demonstrate that the proposed acoustic solutions could also meet certain structural needs.

The paper is organized as follows. The acoustic model is presented in Section 2.1. The studied multilayer configurations, the optimization procedure and the methodology used for the simulations are presented in Section 2.2. Section 2.3 introduces the manufacturing technique. Sections 2.4 and 2.5 describe the methodology used for the experimental characterizations. Manufacturing details and the morphological characteristics of the produced multilayered microchannels are discussed in Section 3.1. The results of the numerical optimizations and the experimental validation are discussed in Section 3.2. The experimental characterization and a trade-off between acoustic absorption and compressive mechanical properties are discussed in Section 3.3. The Section 4 summarizes the most important results and suggests future relevant work.

2. Numerical and experimental procedures

2.1 Acoustic modelling of multilayer microchannels

Figure 1a shows a 3D diagram of the stack of 5-layers composing a multilayer structure. Longitudinal cuts of only 5 layers are shown to make the visualization clearer and easier. The same concept can be extended to materials with a greater number of layers and occupying a larger surface. A

3D schematic of one layer of channels is presented on Figure 1b. Each layer of channels possesses a specific layer thickness, t_i and channel size, D_i. The wall width, W_i is fixed at 200µm, which is the size of the nozzle used for the FFF manufacturing. The mesh pitch of a given layer is the sum of the channel size and the wall width ($P_i = D_i + W_i$). The acoustic behavior of each layer is predicted with the JCAL model [34–36] whereas the acoustic behavior of the multilayered material is predicted with the transfer matrix method (TMM) [37,38].

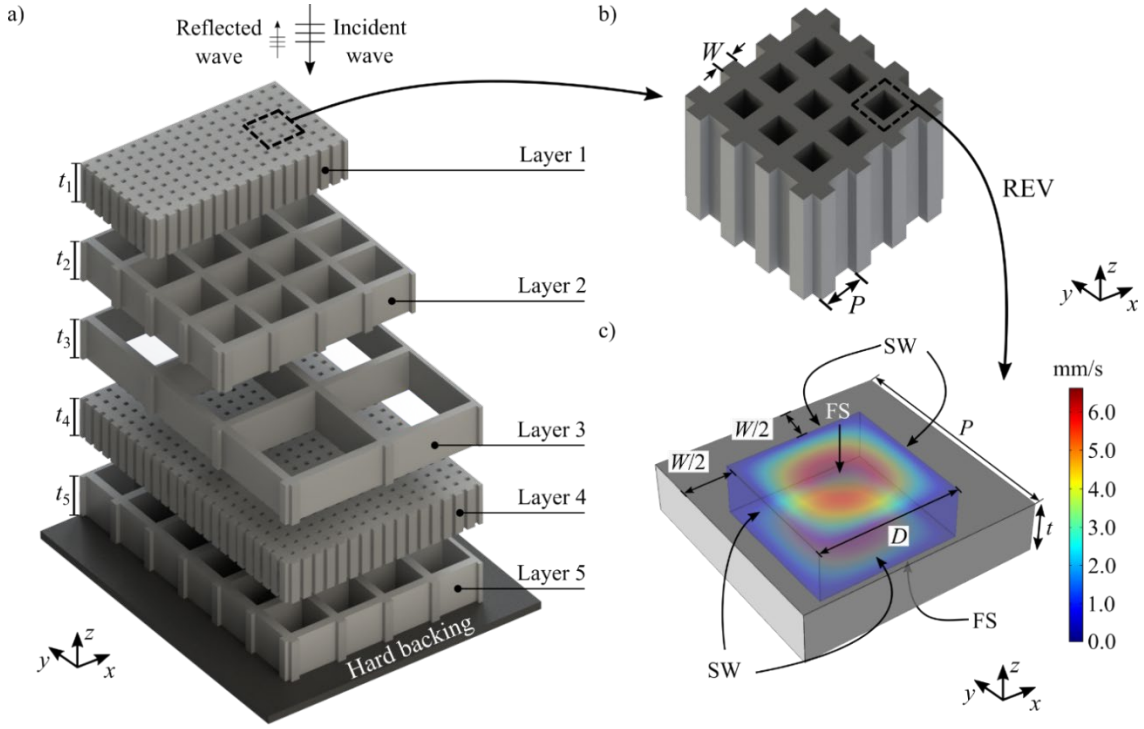

Figure 1 – Acoustic modelling of multilayered microchannels: a) 3D diagram of the stack of 5-layers composing a multilayer structure. b) 3D isometric view of 1 layer of channels. c) simulated velocity field component (z-axis) inside the fluid domain of the channel of the representative elementary volume (REV). SW = Solid walls and FS = fluid surface.

In the JCAL model, the channels are modelled as equivalent fluids and the thermal and viscous losses are accounted for in the complex and frequency dependent bulk modulus, $K_{eq}(D, \mathrm{W}, \omega)$ and density, $\rho_{eq}(D, \mathrm{W}, \omega)$. ω is the angular frequency ($\omega = 2\pi f$, where f is the frequency). Omitting "(D, W)" for the sake of clarity, these quantities are calculated as follows [37]:

$$\rho_{eq} = \frac{\rho_0}{\phi}\left(\alpha_\infty - \frac{\mathrm{j}\nu}{\omega}\frac{\phi}{q_0}\sqrt{1 + \frac{j\omega}{\nu}\left(\frac{2\alpha_\infty q_0}{\phi\Lambda}\right)^2}\right), \quad (1)$$

$$K_{eq} = \frac{\gamma P_0}{\phi}\left\{\gamma - \frac{\gamma - 1}{\left[1 - \frac{\mathrm{j}\nu'}{\omega}\frac{\phi}{q_0'}\sqrt{1 + \frac{j\omega}{\nu'}\left(\frac{2q_0'}{\phi\Lambda'}\right)^2}\right]}\right\}^{-1}. \quad (2)$$

ρ_0, γ, and P_0 are the density, the specific heat ratio and the static pressure of air, respectively. ϕ is the geometrical porosity of a layer of channels (i.e. ratio of the volume occupied by the air to the total volume of the cell). $\nu = \eta/\rho_0$ is the air kinematic viscosity and η is the air dynamic viscosity. $\nu' = \nu/Pr$, is the air thermal diffusivity and Pr is the Prandtl number. j represents the imaginary unit which satisfies $\mathrm{j}^2 = -1$. α_∞ is the high frequency limit of the dynamic tortuosity of a layer of channels. For straight channels with constant cross-section, the tortuosity is equal to one [37]. Λ and Λ' are the viscous and thermal characteristic lengths of the layer of channels, respectively. q_0 and q_0' are the visco-static and the thermo-static permeabilities of the layer of channels, respectively. From Eq. (1) and Eq. (2), the viscous and thermal characteristic frequencies depending on *D* and *W* and the viscous and thermal boundary layers can be calculated as follows [39,40]

$$f_v = \frac{\eta\phi(D,W)}{2\pi\rho_0\alpha_\infty(D,W)q_0(D,W)}, \quad (3)$$

$$f_t = \frac{\eta\phi(D,W)}{\rho_0 2\pi q_0'(D,W)}, \quad (4)$$

$$\delta_v = \sqrt{\frac{2\eta}{2\pi f\rho_0}}, \quad (5)$$

$$\delta_t = \sqrt{\frac{2\kappa}{2\pi f\rho_0 C_P}}. \quad (6)$$

where κ is the thermal conductivity of the air and C_P is the specific heat of the air at constant pressure. Below f_v, the viscous forces are predominant compared to inertial forces, and the flow regime is dissipative. Beyond f_v, the inertial forces are predominant compared to the viscous forces [41]. Below f_t, the regime is isothermal and heat exchange occurs between the air and the channel walls. Beyond f_t, the regime is adiabatic, and there is no heat transfer [41]. f_v, and f_t, are among important parameters to consider when discussing the dissipation mechanisms in porous materials and will be used in section 3.23 to assess the type of regime taking place in multilayered microchannels.

Once the equivalent fluid parameters are known, the acoustic behavior of the channels can be predicted. The equivalent fluid complex wave number k_{eq} and complex characteristic impedance Z_{eq} can be written as follows:

$$k_{eq} = \omega \sqrt{\frac{\rho_{eq}}{K_{eq}}}, \tag{7}$$

$$Z_{eq} = \sqrt{\rho_{eq} K_{eq}}. \tag{8}$$

The JCAL parameters (ϕ, α_∞, Λ, Λ', q_0 and q_0') of a layer of channels are numerically evaluated using the Two-scale Asymptotic Method (TAM) solved with the Finite Element Method (FEM) [42]. In this method, one thermostatic problem, one potential flow problem and one viscous flow (Stokes) problem are solved in the fluid domain of a representative elementary volume (REV). The porosity ϕ, the thermal characteristic length Λ', and the static thermal permeability q'_0 are derived from the solution of the thermostatic problem [2]. The tortuosity σ_∞, and the viscous characteristic length Λ are derived from the solution of the potential flow problem [2]. The static viscous permeability is derived from the solution of the viscous flow (Stokes) problem [2]. For the solution of the three problems, periodic boundary conditions are applied to the fluid surface (FS, on Figure 1c). Regarding the surface of the solid walls (SW on Figure 1c), the following different boundary conditions are used: isothermal boundary condition (i.e., zero excess temperature) to solve the thermostatic problem; no-penetration condition to solve the potential flow problem and no-slip boundary condition to solve the viscous flow (Stokes) problem [43]. The process is carried out for W = 200μm and D varying from 25μm to 15mm to create a database. Steps of 25μm are used in the range from 25μm to 100μm; steps of 200μm and 2mm are used from 100μm to 1mm and from 1mm to 15mm, respectively. The database is used to find equations correlating each JCAL parameter to D. The equations are found using the Matlab curve fitting application toolbox version 3.5.9. The dashed black square on Figure 1b highlights the surface of the REV of a layer of channels. The TAM method is implemented in the commercial FEM software Comsol Multiphysics. For the sake of conciseness, theory and details of the TAM are not presented but can be found in [42]. Detailed information on the treatment and numerical implementation of the TAM, including benchmark examples can be found on [43]. Figure 1c shows the simulated velocity field of the air inside a channel (D = 300μm; W = 200μm and t = 100μm). The dark blue color indicates zero air velocity at the boundaries and the dark red indicates maximum velocity (~ 6mm/s) at the center of the channel.

The TMM [37] is used to predict the acoustic properties of the multilayered material. In this method, each layer of channels is represented by a 2 × 2 matrix expressed in terms of the thickness of the layer, t_i, its equivalent fluid wave number, k_{eq}^i, and its characteristic impedance, Z_{eq}^i,

$$\mathrm{TM^i} = \begin{bmatrix} \cos(k_{eq}^i \cdot t_i) & i \cdot Z_{eq}^i \cdot \sin(k_{eq}^i \cdot t_i) \\ \frac{i}{Z_{eq}^i} \cdot \sin(k_{eq}^i \cdot t_i) & \cos(k_{eq}^i \cdot t_i) \end{bmatrix}. \quad (9)$$

The matrix of the multilayer treatments are then calculated by multiplying the transfer matrix of each layer of channels,

$$\mathrm{TM} = \prod_{i=1}^{N} \mathrm{TM}^i. \quad (10)$$

The surface impedance for rigidly backed multilayer microchannels (absorption problem) receiving plane acoustic waves with normal incidence are calculated with the total transfer matrix $Z_s(\omega, D, W) = \frac{TM(1,1)}{TM(2,1)}$. The normal incidence complex sound reflection coefficient, $R(\omega, \mathrm{W}, D)$, is then calculated with Eq. (11),

$$R(\omega, D, W) = \frac{Z_s - Z_0}{Z_s + Z_0}. \quad (11)$$

Z_0 is the characteristic impedance of the air. The sound absorption coefficient, α, is finally computed as $\alpha(\omega, D, W) = 1 - |R(\omega, D, W)|^2$. The JCAL and TMM acoustic models are implemented on Matlab R2019a.

2.2 Sound absorption coefficient optimization

2.2.1 Frequency ranges and studied configurations

The target frequency ranges (FR), the number of layers and the thickness of each layer investigated in this work are presented. Figure 2a shows the simulated sound absorption coefficient of optimal 1-layer microchannels with 30mm thickness (D = 290µm; W = 200µm and ϕ = 0.35). The circle indicates the theoretical QWRF = 2833Hz (i.e., $f = c/4L$ for c = 340mm/s and T = 30mm). The black cross indicates the absorption peak frequency ($f_{peak} \sim$ 2400Hz). The uniform structure presents a subwavelength absorption peak since the ratio first absorption peak wavelength to structure thickness, λ_{peak}/T is greater than 4. The 500-2400Hz frequency range was chosen to improve the performance at low frequencies ($f < f_{peak}$). The 2400-6500Hz frequency range was chosen to improve the performance at high frequencies ($f > f_{peak}$). The 500-6500H frequency range was chosen to improve the performance at low and high frequencies ($f < f_{peak}$ and $f > f_{peak}$). The same methodology can be applied to any other frequency range of interest. Concerning the layers arrangement, schematics of the 5 configurations

investigated are shown in Figure 2b-f. Figure 2b illustrates the uniform configuration (1-layer) which contains microchannels with the same size D throughout the material thickness, T =30mm. Figure 2c shows the 2-layers configuration. It is composed of a top layer (facing incident wave) with microchannels of size D_1 and a thickness of t_1 = 1mm and a bottom layer of microchannels of size D_2 and a thickness of t_2 = 29mm. Figure 2d, e and f present the configurations with 5-, 10- and 30-layers, respectively. They are composed of layers of identical thickness t_i = 6, 3 and 1mm, respectively. All structures are in absorption configurations (i.e., with a rigid backing illustrated by the black rectangles). For the sake of simplicity, only the results of the optimizations for uniform and 30-layers microchannels are presented in Section 3.2. The case of 30-layers is the one with the greater thickness resolution (i.e., t_i = 1mm instead of t_i = 3mm for the 10-layers or t_i = 6mm for the 5-layers) and leads to better results. The complete analysis is available in Appendix A1. Additional optimizations with variable N, t_i and D_i and variable t_i and D_i for fixed numbers of layers were performed for the FR 500-6500Hz. The results are available in Appendix A2.

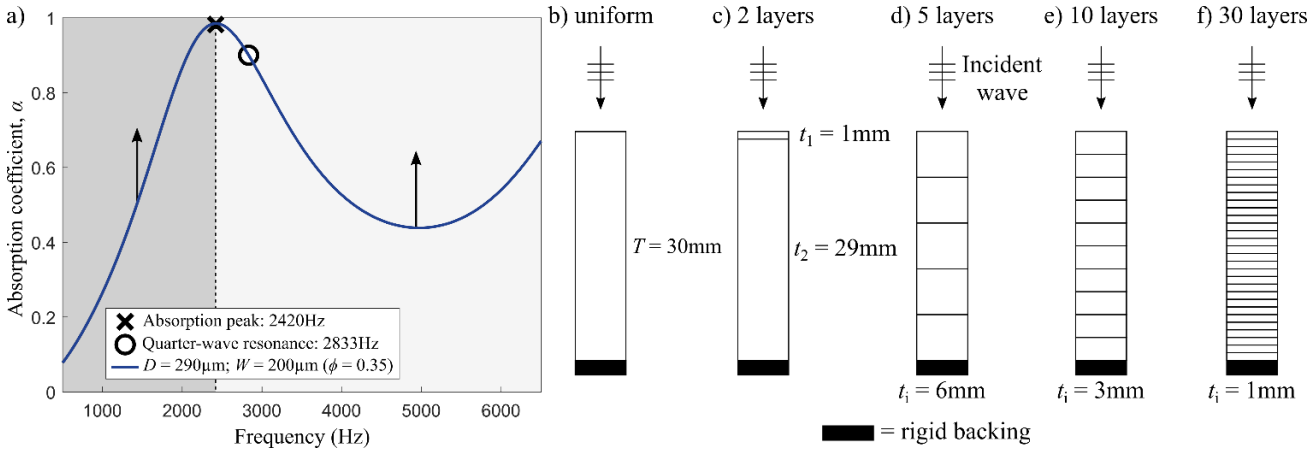

Figure 2 – Frequency ranges and studied configurations: a) sound absorption coefficient of the optimized uniform microchannels. The frequency ranges are: 500-6500Hz; 500-2400Hz and 2400-6500Hz. b-f) Schematics of the investigated configurations: b) uniform; c) 2-layers; d) 5-layers; e) 10-layers; and f) 30-layers.

2.2.2 Optimization of the sound absorption coefficient

The objective of the optimization procedure is to find the channels size, D_i of each layer leading to multilayered structures providing effective sound absorption coefficient in the targeted frequency ranges. The optimization process is performed numerically using the simplex Nelder-Mead iterative optimization method [44]. The numerical method finds the value of D_i that reduces the following cost function

$$J(D,\omega) = \sum_{\omega} K(\omega)\left(\left|\mathcal{R}(D,\omega) - \mathcal{R}_{obj}(\omega)\right|^2\right). \quad (12)$$

$\mathcal{R}(\omega)$ is the reflexion coefficient, $\mathcal{R}_{obj}(\omega) = 0$ and $K(\omega)$ is the frequency weighting function used to define the target frequency ranges. For the purpose of the present work, $K(\omega) = 1$ on the chosen target frequency range and zero outside of the range. Eq. (12) enables the design of multilayer treatments corresponding to reduced reflection coefficient for specific frequency ranges and fixed wall width. The optimizations are performed for D_i varying between 100µm and 15mm. The lower bound of 100µm is dictated by the limitations of the manufacturing capabilities while channel sizes above the higher bound of 15mm lead to poor acoustic absorption and mechanical properties. For each configuration, the iterative optimization method is used to numerically solve the optimization problem 500 times with different random initial estimations for D_i. The 500 results are compared and the one leading to the lowest cost-function is considered the best solution. The stopping criterion of the numerical optimization is given by the norm between the current and previous iterations, $\varepsilon < 10^{-7}$. To reduce the computation time of the numerical optimization, the FR are sampled with 1 point per 100Hz. Therefore, 20, 42 and 61 frequency points are used to sample FR 500-2400Hz, 2400-6500Hz and 500-6500Hz, respectively. The optimization procedure is implemented on Matlab R2019a.

2.2.3 Methodology of the simulations

For all simulations and optimizations, the thickness of the multilayered structures is 30mm and the absorption average $\bar{\alpha}$ is used as the objective parameter to compare the configurations. For all configurations and FR, the absorption average is calculated for frequencies between 500 and 6500Hz with 6000 points in the frequency domain, which represents a frequency step of 1Hz. Moreover, the noise reduction coefficient (*NRC)* is used to compare the absorption of multilayered microchannels with other published work since the absorption average is not available. The *NRC* was calculated based on the available sound absorption curves using the following equation [10]:

$$NRC = \frac{1}{4}[\alpha_{250} + \alpha_{500} + \alpha_{1000} + \alpha_{2000}]. \quad (13)$$

The average porosity was used to estimate the percentage of air of the multilayer microchannels. The percentage of air is calculated as follows:

$$\bar{\phi} = \frac{1}{L} \sum_{i=1}^{Number\ of\ layers} l_i \cdot \phi_i. \quad (14)$$

The porosity of each layer of channels, ϕ_i is given by

$$\phi_i(D_i, W) = \frac{D_i^2}{(D_i + W)^2}. \tag{15}$$

The experimental error percentage is calculated as follows

$$e = \frac{1}{6000} \sum_{i=500}^{6500\text{Hz}} \left| \frac{\alpha_{experimental}(f_i) - \alpha_{theoretical}(f_i)}{\alpha_{theoretical}(f_i)} \right| \times 100. \tag{16}$$

The absorption of the multilayered microchannels optimized for the FR 500-6500Hz is compared to the one of the melamine foam (trade name BASF Basotect®) and the glass wool which are porous materials with high and broadband absorption capabilities. The absorption curve of the melamine foam and glass wool are obtained by simulation with the JCAL model [34–36,45].

2.3 Manufacturing procedure

Samples of multilayered microchannels are produced using the FFF 3D printer Raise 3D Pro2 equipped with a 0.2mm nozzle. The printing layer height is set at 0.1mm. Red and Black Raise3D® premium polylactic acid (PLA) with 1.75mm filament diameter is used. Extrusion and bed temperatures are set at 235°C and 50°C, respectively. The printing speed is set to 27mm/s.

A FFF based fabrication technique called "Zigzag" is used to produce multilayered microchannels. Figure 3a shows a schematic of the Zigzag pattern. Channels are the result of the deposition of filaments along the zig-zag trajectory illustrated by the white points (p_1, p_2, …, p_n) and arrows. The FFF Zigzag pattern is implemented in Matlab R2019a.

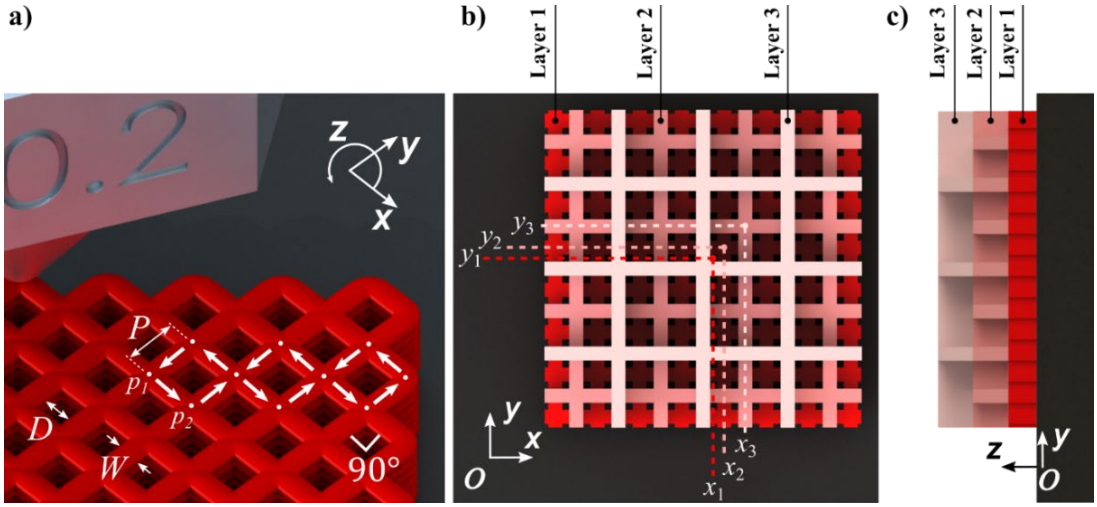

Figure 3 – Manufacturing of multilayer structures via FFF: a) Schematic of the Zigzag technique used to produce each layer of channels. b) Schematic of a 3 layers structure with 3 different channels size. c) Side view showing the staking of the channels.

The size of each layer of channel must be a multiple of the smallest channels size to avoid channel obstruction. Specifically, the channel size for each layer must comply with following rule

$$D_i = \mathrm{P}_1 \cdot 2^{n_i - 1} - W_i. \quad (17)$$

i = 1 for the smallest channels. n_i is the integer exponent of a layer that is equal or greater than 1, P_1 is the mesh pitch of the smallest channels. To correctly apply Eq. (17) it is necessary to consider $n_1 = 1$ for the layer with the smallest channels, $n_2 = 2$ for the layer with P_2 twice as large as P_1 and so on. Figure 3b illustrates the strategy used for the stacking of the channels. Figure 3c shows a side view of the channels staking. The position of the center of the channels of each layer in the 3D-printing bed is given in the (X, Y) axes. Only positive coordinates are used, and the origin O (0, 0) is the rest position of the 3D-printing nozzle. The user enters the position of the sample in the 3D-printing bed (x_1, y_1). This position is assigned to the center of the channel located at the middle of the layers with the smallest channels (the layer 1 of the structure on Figure 3b and c). The position of all other channel centers for a given layer i (x_i, y_i) – with i an integer greater than 1 – are calculated according to equations (18) and (19) (e.g., the layer 2 and 3 of the structure on Figure 3b).

$$x_i = x_1 + \sum_{k=2}^{i} \frac{P_{k-1}}{2}, \quad (18)$$

$$y_i = y_1 + \sum_{k=2}^{i} \frac{P_{k-1}}{2}. \quad (19)$$

2.4 Acoustic and mechanical experimental characterization

The experimental sound absorption coefficient of 30mm thick cylindrical samples is measured in a 30mm diameter impedance tube equipped with two microphones in absorption configuration – i.e. hard backing behind the sample – according to the ASTM E1050 [46] and ISO 10534-2 [47] standards. The samples are printed with a solid border to ensure tight fitting in the tube and to prevent sound leakage. Figure 4a shows a schematic of the measurement set-up with the 30 mm-diameter impedance tube. Figure 4b shows a schematic of a multilayer sample. Figure 4c shows the samples border detail. All measurements are made in the 500-6500Hz frequency range. The sound level is 94dB.

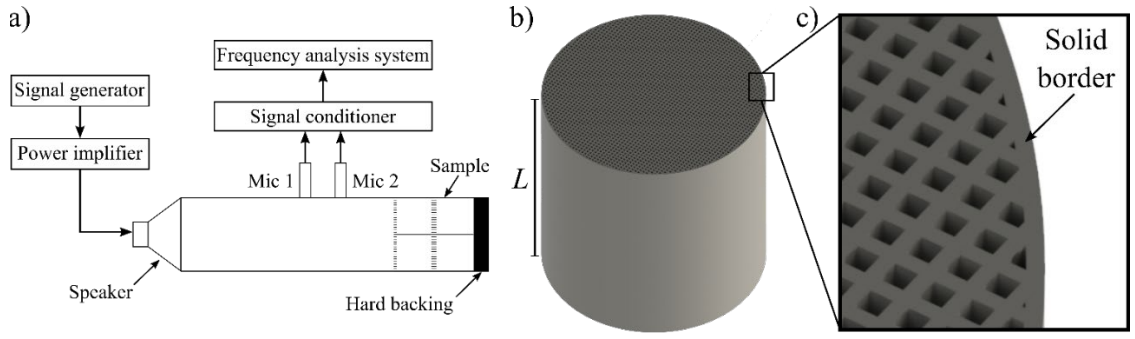

Figure 4 – Measurement of the sound absorption coefficient: a) Measurement set-up with the 30 mm-diameter impedance tube (ASTM E1050 and ISO 10534-2) [1]; b) Schematic view of a sample used on the impedance tube; c) Schematic view highlighting the solid border of the sample.

Compression tests were performed on 3D printed acoustic samples. The mechanical properties are calculated according to ASTM standard D695 [48]. The compression tests are performed on an electromechanical material testing system (MTS Instron 1362) equipped with 20kN load cell (model number 2518-602) for tests on multilayered microchannels material and 100kN load cell (model number 2519-611) for tests on uniform microchannels. The tests are controlled in displacement with a crosshead speed of 1.8 mm/min. All samples are printed with PLA. To consider the variability of the manufacturing on the acoustic and mechanical properties, all tests were performed on at least three samples produced under the same manufacturing conditions. The mechanical properties of the multilayered microchannels optimized for the FR 500-6500Hz is compared to the one of the melamine foam (BASF Basotect®) and Duocel® Aluminum Foam.

2.5 Morphology and mass experimental characterization

An optic microscope (Olympus SZX-12) and the software ImagePro Plus are used to measure the channels size, $D_{measured}$ of the 3D printed structures. 30 measurements of $D_{measured}$ are taken in 10 channels for each sample. The mass of the 3D printed acoustic samples and the melamine foam is measured with the A&D Weighing lab balance (GH-200). The mass is used to calculate the density of the samples, $\rho = m/V$, where V is $\pi \cdot 15^2 \cdot 30\text{mm}^3$.

3. Results and discussions

3.1 FFF manufacturing of multilayered microchannels

3.1.1 Manufacturing of microchannels

Figure 5a and b present the top and side pictures of microchannels produced with $D_{desired}$ = 100µm. $\overline{D}_{measured}$ = 99µm which represents only 1% relative error. No transverse porosity was observed on the microscopic images of Figure 5b and c. Microchannels with $D_{desired}$ = 75 and 50µm were also manufactured but the channels were partially blocked due to insufficient machine precision. Therefore, the minimum size of channels that can reliably be obtained with the Zigzag technique and the equipment used in this work is found to be 100µm. 100µm perforations was proven to be in the optimal range of perforations size of micro-perforated panels in previous work [27,28]. Besides micro-perforated panels, structures with 100µm perforations could be a good alternative to the wire mesh usually added on the top of acoustic liners to adjust the impedance [49], and the septum typically used between honeycomb cells in 2 degree of freedom (DoF) acoustic liners. The advantage of using the Zigzag technique is that the treatment, acoustic liners for example, could be produced in one manufacturing step avoiding any subsequent parts assembly. Microchannels treatment with the thickness and the pore size presented in this work cannot be obtained via SLA because of the restricted laser beam spot size that polymerizes the resin on the surroundings of the desired areas making it difficult to remove it from inside the microchannels. This issue was also raised in [11] during the manufacturing of TPMS cells. Yet, the manufacturing process presents some drawbacks. The 100µm microchannels cross-sections is elliptical rather than square, and the distribution of microchannels size is not uniform as seen on Figure 5a. Moreover, the surface of the microchannel walls is rather wavy as shown on Figure 5b and c. The acoustic model considers perfect square cross-sections and smooth wall. The waviness induced by 3D-printing increases the porosity and the tortuosity of microchannels [51]. Moreover, it reduces the viscous permeability [51]. These changes generally contribute to increased sound absorption [51]. Besides the non-perfect microstructure, the main drawback is the manufacturing time (10 hours to produce 30mm-thick cylindrical samples with 30mm diameter of 30-layers optimized microchannels). Long printing time is an impediment to large scale manufacturing of structures with fine features. High-speed or multinozzle additive manufacturing techniques may be applied to overcome this problem [51,52].

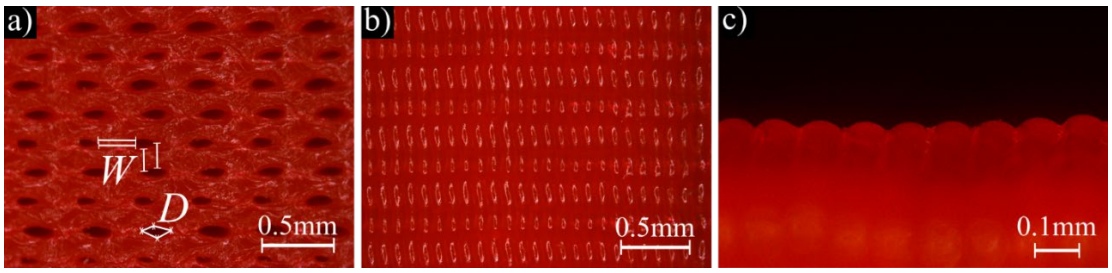

Figure 5 – Optical microscopic images of microchannels ($D_{\text{desired}} = 0.1$mm): a) top picture; b) side picture; c) detail of the waviness of the walls of FFF manufactured microchannels.

3.1.2 Manufacturing unsupported layer of channels

The optimization of multilayered microchannels leads to the stacking of successive layers of different channels size. To 3D print these unsupported structures, four thin layers of transversal straight filaments were used as supports. Figure 6a shows in detail small channels (0.6mm) printed over 0.4mm-thick supports. The support filaments rest on the edges of the samples and on the walls of the previously printed channels. The spacing between the support filaments is equal to the size of the channels they will support. Additionally, to avoid obstruction, the support filaments are aligned with the walls of the channels they will support. The thickness of the layers with larger channels is reduced to compensate for the support addition because larger channels contribute less to the visco- and thermal losses than the resistive microchannels. The total thickness of the samples remains 30mm. Figure 6b shows the interior of a cut 30mm-thick acoustic sample with 30-layers. Figure 6c shows the detail of the upper part of the cut sample. It can be seen that channels of different sizes are correctly stacked with the developed technique.

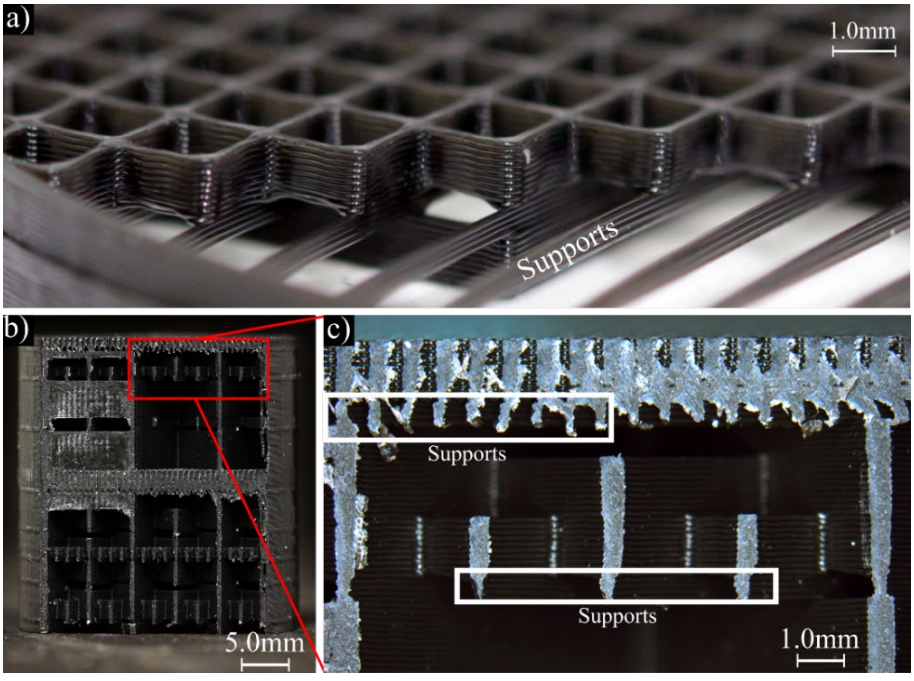

Figure 6 – Manufacturing of multilayered microchannels: a) detail of small channels (0.6mm) printed over 0.4mm-thick supports; b) interior of a cut 30mm-thick acoustic sample with 30-layers; c) detail of the upper part of the cut sample

3.2 Numerical optimization and experimental validation

3.2.1 Frequency range 500-2400Hz

Figure 7a presents the sound absorption coefficient of 30-layers microchannels optimized for FR 500-2400Hz (black curves). The dash-dotted blue curve corresponds to uniform microchannels (i.e., single layered with D = 0.29mm). The histograms show the average absorption for each case. Figure 7b presents the schematic view of the 30-layers optimized structure. The thickness of each layer is fixed 1mm. The channels sizes are optimized, and the solution contains five different channel sizes. Some channel sizes are repeated in successive layers; therefore the 30-layers structure is equivalent to a 19-layers structure. D = 0.1mm in layers t_1, t_2 and t_{12}. D = 0.4mm in t_{11}. D = 2.2mm in t_{10}, t_{16}, t_{23}, t_{28} and t_{29}. D = 4.6mm in t_3, t_4, t_5, t_6, t_{13}, t_{14}, t_{18}, t_{19}, t_{21}, t_{22}, t_{25}, t_{26} and t_{30}. D = 9.4mm in t_7, t_8, t_9, t_{15}, t_{17}, t_{20}, t_{24} and t_{27}. The percentage of air $\bar{\phi}$, the frequency f_1 and the absorption coefficient α_1 at the first resonant peak, λ_{peak}/T and the experimental error percentage e, are listed in Table 1. As shown on Figure 7b, the 30-layers is equivalent to a two degree-of-freedom (DoF) liner composed of two resistive layers or micro-perforated panels (MPP) with D_1 = 0.1mm and permeable layers with channels larger than 0.4mm. Because of the two resistive layers, the 30 layers structure present two absorption peaks. The 1st absorption peak (1630Hz) is produced by the 1st resistive layer and the 2nd absorption peak ($\sim$ 6000Hz) is produced by the 2nd resistive layer. In this work, the microchannels are called resistive when the magnitude of the air flow resistivity ($\sigma = \eta/k_0$) is 10^5 Nsm^{-4}. According to the simulations, this happens when D < 170μm. On the other hand, when $D \geq$ 170μm the channels are called permeable. In this sense, only the smallest channels of the optimized multilayered structures are considered resistive. The experimental absorption averages are $\bar{\alpha}$ = 0.75 and NRC = 0.49. The experimental first absorption peak frequency of the 30-layers structure is 1695Hz. This is 1138Hz lower than the quarter wave resonance frequency (QWRF). Multilayered microchannels are lighter and present better absorption capabilities than uniform microchannels. The absorption average of the 30-layers structure is 13% higher than the one of uniform microchannels. The percentage of air of the 30-layers structure is 2.7 times higher than the one of uniform microchannels.

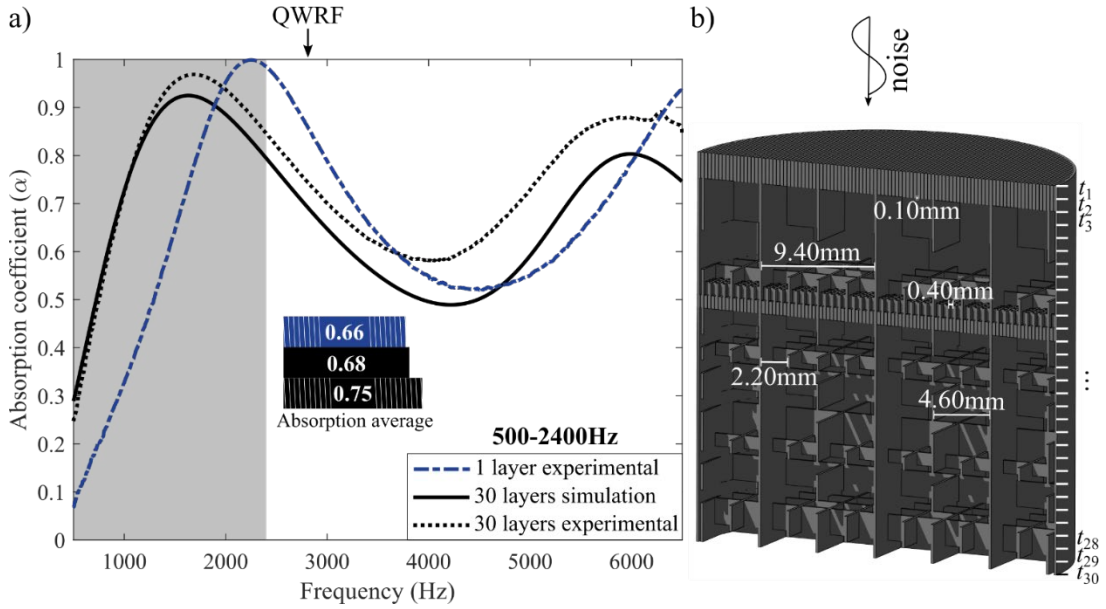

Figure 7 – Results of optimization for the frequency range 500-2400Hz: (a) Comparison of the absorption coefficient of the 1- and 30-layers microchannels (b) Scheme of the 30-layers configuration.

Table 1 – Percentage of air $\bar{\phi}$, frequency f_1 and absorption coefficient α_1 at the first resonant peak, λ_{peak}/T and the percentual experimental error, e of structures optimized for the frequency range 500-2400Hz

Configuration	Percentage of air, $\bar{\phi}$ (%)	Frequency at first peak, f_1 (Hz)	Absorption at first peak, α_1	λ_{peak}/T	e (%)
1-layer experimental	30	2260	1.0	5.0	-
30-layers simulation	82	1630	0.92	6.9	9.2%
30-layers experimental	82	1695	0.97	6.7	

3.2.2 Frequency range 2400-6500Hz

Figure 8a presents the sound absorption coefficient of structures optimized for FR 2400-6500Hz. The dash-dotted blue curve corresponds to uniform microchannels (i.e., single layered with D = 0.29mm). Figure 8b presents the schematic view of the 30-layers optimized structure. The thickness of each layer is fixed 1mm. The solution contains four different channels sizes. Some channel sizes are repeated in successive layers; therefore the 30-layers structure is equivalent to a 23-layers structure. D = 0.11mm in layers t_{12}, t_{22}, t_{24} and t_{26}. D = 1.04mm in t_1, t_3, t_6, t_7, t_{16}, t_{19}, t_{20}, t_{23}, t_{28} and t_{29}. D = 2.28mm in t_2, t_4, t_5, t_{10}, t_{18}, t_{25} and t_{30}. D = 4.76mm in t_8, t_9, t_{11}, t_{13}, t_{14}, t_{15}, t_{17}, t_{21} and t_{27}. $\bar{\phi}$, f_1, α_1, λ_{peak}/T and e are listed in Table 2. Contrarily to 500-2400Hz structures, multilayered microchannels designed for higher absorption in the 2400-6500Hz frequency range present 11 permeable top layers facing the wave and resistive back layers (schemes of Figure 8b). The top permeable layers increase the

material thickness reducing the frequency of the absorption peak from f_{19} = 3370Hz to f_{30} = 3085Hz, since the frequency of the peak depends on the material thickness ($f \sim c/4T$). The experimental absorption averages are $\bar{\alpha}$ = 0.82 and NRC = 0.33. The absorption average of the 30-layers structure is 24% higher than the one of the 1-layer structure. The absorption of the 30-layers structure is almost perfect in the FR. Additionally, the 30-layers structure present percentage of air ($\bar{\phi}$ = 73%) 2.4 higher than the uniform microchannels.

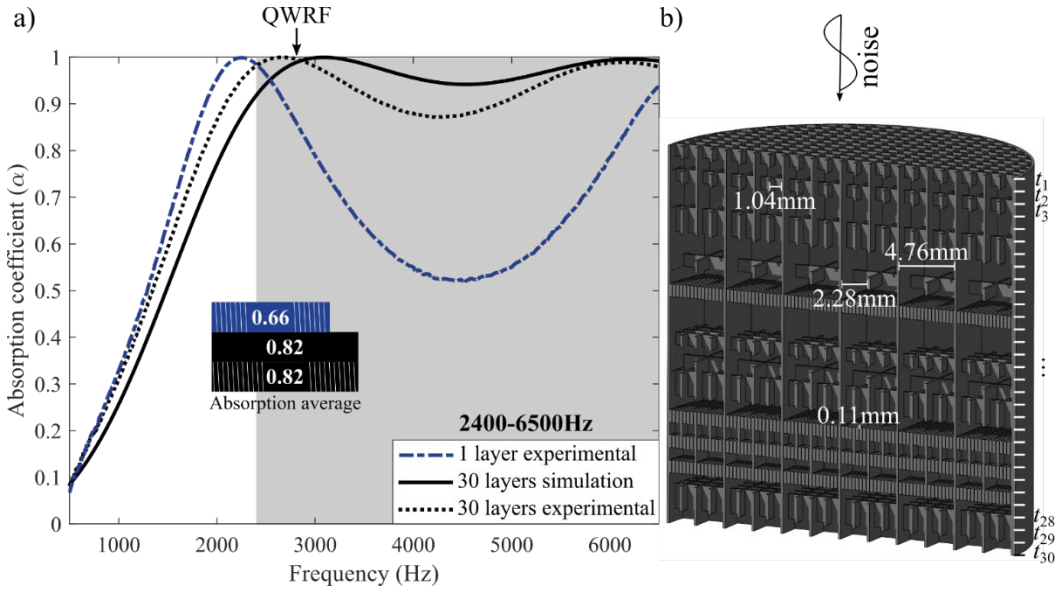

Figure 8 – Results of optimization for the frequency range 2400-6500Hz: (a) Comparison of the absorption coefficient of the multilayer and uniform microchannels (b) Scheme of the 30-layers configuration.

Table 2 - $\bar{\phi}$, f_1, α_1, (λ_{peak}/T) and e of structures optimized frequency range 2400-6500Hz

Configuration	Percentage of air (%)	Frequency at first peak, f_1 (Hz)	Absorption at first peak, α_1	λ_{peak}/T	e (%)
1-layer experimental	30	2260	1.0	5.0	-
30-layers simulation	73	3085	1.0	3.7	7.8
30-layers experimental	73	2664	1.0	4.3	

3.2.3 Frequency range 500-6500Hz

Figure 9a presents the sound absorption coefficient of structures optimized for FR 500-6500Hz. The dash-dotted blue curve corresponds to uniform microchannels (i.e., single layered with D = 0.29mm). Figure 9b presents the schematic view of the 30-layers optimized structure. The thickness of each layer is fixed 1mm. The solution contains six different channels sizes. Some channel sizes are repeated in successive layers; because of that the 30-layers structure is equivalent to a 20-layers structure. D = 0.10mm in layers t_1, t_{15} and t_{16}. D = 0.40mm in t_{23}. D = 1.00mm in t_4, t_{28} and t_{29}. D = 2.20mm in t_3,

t_{10}, t_{19}, t_{20}, t_{22}, t_{24}, t_{25} and t_{27}. D = 4.60mm in t_5, t_6, t_7, t_8, t_9, t_{11}, t_{17}, t_{26} and t_{30}. D = 9.40mm in t_2, t_{12}, t_{13}, t_{14}, t_{18} and t_{21}. $\bar{\phi}$, f_1, α_1, λ_{peak}/T and e are listed in Table 3. The 30-layers structure (black curves and schemes, respectively) presents two absorption peaks typical of two DoF liners. Therefore the 30-layers treatment can be reduced to a 4-layers one (2 resistive layers backed by 2 permeable layers). The experimental absorption averages of the 30-layers structure are $\bar{\alpha}$ = 0.86 and NRC = 0.46. The 30-layers structure exhibits also subwavelength behavior (experimental λ_{peak}/T = 5.9) and broadband acoustic absorption with the experimental first peak located at 1920Hz. The absorption curves of melamine foam and glass wool (orange and pink dashed curves) are found to be lower than multilayered microchannels optimized for the 500-6500Hz frequency range.

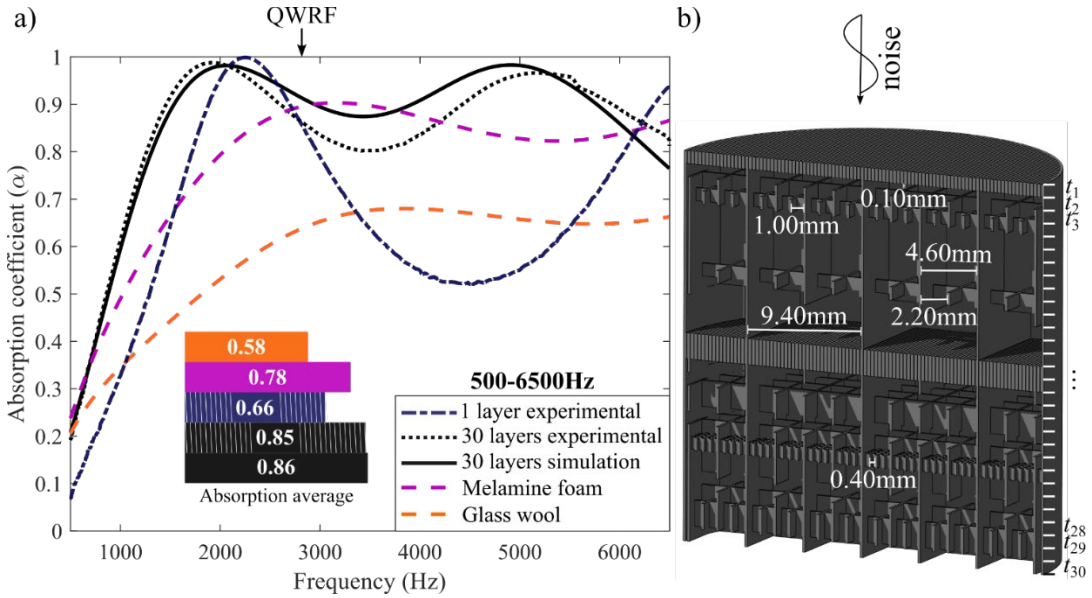

Figure 9 – Optimization results for the frequency range 500-6500Hz: (a) Comparison of the absorption coefficient of the multilayer and uniform microchannels (b) Scheme of the 30-layers configuration.

Table 3 - $\bar{\phi}$, f_1, α_1, (λ_{peak}/T) and e of structures optimized for the frequency range 500-6500Hz

Configuration	Percentage of air (%)	Frequency at first peak, f_1	Absorption at first peak, α_1	λ_{peak}/T	e (%)
1-layer experimental	30	2260Hz	1.0	5.0	-
30-layers simulation	79	2075Hz	0.98	5.5	4.3
30-layers experimental	79	1920Hz	0.99	5.9	

The experimental and simulated resistance and reactance at around 2000Hz are not far from $Z = 1\rho c$ and Im(Z) = 0, which explains the near perfect sound absorption ($\alpha \sim 1.0$) at the absorption peak. Moreover, the simulated impedance fits well the experimental data from ~500Hz to ~2500Hz which explains the

good match between the experimental and the simulated sound absorption coefficient in this frequency range. For all FR the experimental acoustic absorption is in good agreement with the numerical predictions. The experimental error does not reach 10% with respect to the simulations. The shift comes from the manufacturing defects. The surface waviness affects the JCAL parameters, which consequently changes the absorption. Specifically, the presence of waviness on the microchannels increases the porosity and the tortuosity [50,53]. It decreases the static viscous permeability [50,53]. As a consequence, the waviness tends to increase the sound absorption [50,53] which explains why the experimental absorption is, in general, higher than the simulated one. Nevertheless, the theory does not overestimate the absorption and is valid to design multilayered microchannels with increased absorption. Table 4 lists the values of f_v and f_t for the 1-, and 30-layers microchannels with channel sizes optimized for the frequency range 500-6500Hz. The viscous and thermal losses are predominant for the microchannels with D = 0.1mm, since f_v and $f_t \sim$ 4000Hz, which is relatively high within the full studied frequency range [41]. The inertial and adiabatic regime are predominant for all other channels composing the 30-layers microchannels [41]. The values of f_v and f_t for these other layers suggest that the dissipation of the 30-layers microchannels is predominantly visco-inertial and that thermal dissipation appears only in layers with D = 0.1mm. On the other hand, the sound absorption of the 1-layer microchannel material is predominantly visco-inertial, since f_v and $f_t \sim$ 860Hz which is relatively low within the full studied frequency range. The variation between resistive layers (with visco and thermal dissipations) and permeable layers (with inertial dissipation) contributes to increasing the sound absorption of multilayer microchannels. From 1500Hz and 3000Hz, the viscous (δ_v) and thermal (δ_t) boundary layers vary from $0.057\text{mm} < \delta_v < 0.041\text{mm}$ and $0.068\text{mm} < \delta_t < 0.048\text{mm}$. Therefore, with the specific microchannel size D = 0.1mm found by the optimization procedure, the viscous and thermal layers fill up most of the channels, leading to high viscous and thermal dissipation and high sound absorption [3]. These conclusions also apply to other structures (optimized for 500-2400Hz and 2400-6500Hz).

Table 4 - $\boldsymbol{f_v}$ and $\boldsymbol{f_t}$ for the channels size of 1- and 30-layers microchannels optimized for the frequency range 500-6500Hz

	30-layers microchannels						1-layer microchannels
	D (mm)						D (mm)
	0.10	0.40	1.00	2.20	4.60	9.40	0.29
$\boldsymbol{f_v}$ (Hz)	4042	441	71	15	3	1	860
$\boldsymbol{f_t}$ (Hz)	3680	442	71	15	3	1	866

As summarized in Table 5, the developed multilayered microchannels offer better acoustic properties than other 3D-printed periodic porous structures. The excellent acoustic properties of the multilayered microchannels result from the microstructure optimization routine combined with the simple and robust FFF based manufacturing that allows to obtain thin walls and unobstructed microchannels through the desired thickness.

Table 5 – *NRC* of 30-layers structures compared to the state of the art of 3D printed PPS

	T (mm)	*NRC*
FFF 30-layers multilayer microchannels (500-6500Hz)	30	0.46
FFF uniform microchannels	30	0.36
DWI uniform micro-lattices [1]	30	0.2
DWI optimally graded micro-lattices [30]	30	0.4
µSLA 2-layers MPP with oblique perforations [26]	30	0.22
DLP and SLM Kelvin cell metamaterial [12]	30	0.29, 0.4, respectively
FFF micro-helix metamaterial [9]	30	0.18

3.3 Trade-off between acoustic absorption and mechanical properties

Compression and acoustic tests were performed on uniform microchannels and 30-layers microchannels with improved absorption for the FR 500-6500Hz. The geometry details of the 30-layers structure are presented on section 3.2.3. Four additional configurations of 4-layers structures were also tested. The choice of these configurations was motivated by the fact that 4-layers are the required minimum to obtain a two DoF liner. The starting point for the 4-layers structure is the optimized 30-layers microchannels in which the two resistive layers are kept unchanged, and the more permeable layers are replaced by two layers. The channels size of the two resistive layers are maintained constant (D_1 and D_3 = 100µm) while the channels size of the 2 permeable layers D_2 and D_4 are changed according to Eq. (17) with P_1 = 300µm and different exponents. The exponent n_i and the respective channels size of the permeable layers are listed on Table 6.

Table 6 - Exponent n_i and respective channels size of the permeable layers

Exponent of permeable layers	Channels size of permeable layers, D_2 and D_4
n = 6 (pink curve)	9.40mm
n = 5 (green curve)	4.60mm
n = 4 (orange curve)	2.20mm
n = 3 (red curve)	1.00mm

The thicknesses of the resistive layers are t_1 = 1mm and t_3 = 2mm and the thicknesses of the permeable layers are t_2 = 13mm and t_4 = 14mm. Simulations of the sound absorption coefficient of the 4-layers

structures are available on the Appendix A3. The experimental stress-strain and the sound absorption coefficient curves are presented on Figure 10a and b. Schematics of the longitudinal section of the tested structures are shown on Figure 10c. Table 7 gathers the thickness T, density $\rho = m/V$, absorption average $\bar{\alpha}$, compressive elastic modulus E_c, specific elastic modulus E_c/ρ, yield strength σ_y and specific yield strength, σ_y/ρ of 1-, 4-, and 30-layers microchannels, melamine foam and Duocel® Aluminum Foam. Optimal uniform microchannels present the highest yield strength ($\sigma_y = 33$MPa). The compressive modulus of uniform microchannels is more than five times the aluminium foam (Duocel®) and more than 2500 times the melamine foam. Although the acoustic properties of the multilayered microchannels are quite similar, there is an important difference in the mechanical properties. As expected, the compressive modulus and the yield strength decrease with increasing channels size of the permeable layers. The best trade-off between the acoustic and the mechanical properties is obtained with the n = 3 configuration (red curves and scheme on Figure 10). The n = 3 configuration offers high broadband sound absorption with average absorption of $\bar{\alpha}$ = 0.85 and the highest specific mechanical properties (E_c/ρ = 5088MPa cm^3/g and σ_y = 98MPa cm^3/g). Therefore, the n = 3 configuration might be an interesting solution for applications where structural and acoustic performance are of interest such as the transport industry. Although liners with two DoF are already used as sound absorbers in aircraft engines, a comprehensive work including an optimization procedure and a manufacturing technique able to produce in one step liners with 1 or more DoF including perforated plates with perforations of up to 100µm was never reported. In addition, additive manufacturing allows greater flexibility for the dimensions of each layer and may be used to produce nonplanar or large scale parts [54,55].

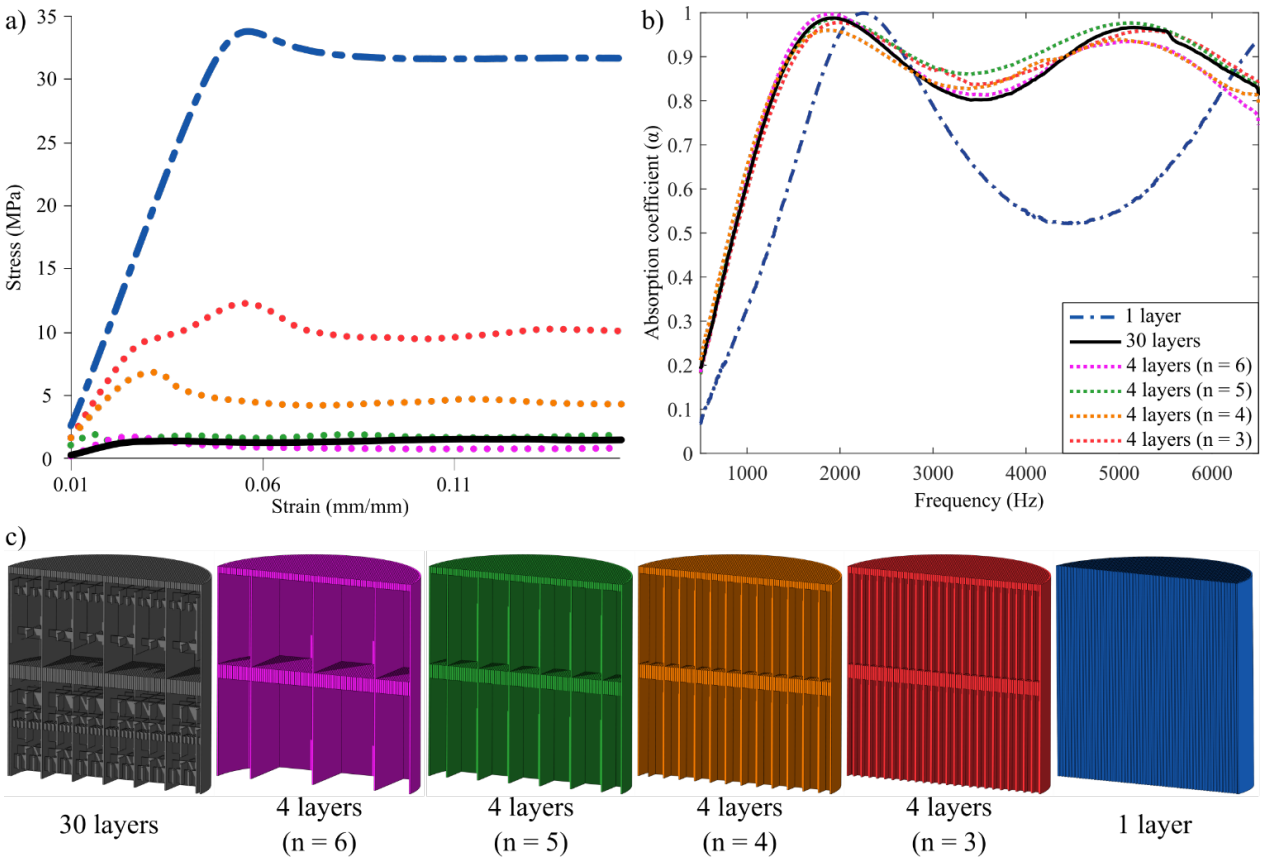

Figure 10 – Experimental mechanical and acoustic properties of 1-, 4- and 30-layers optimized structures (500-6500Hz): a) stress-strain curves; b) sound absorption coefficient curves; c) schematics of the tested materials.

Table 7 – T, $\rho = m/V$, $\bar{\alpha}$, E_c, E_c/ρ, σ_y and σ_y/ρ of 1-, 4- and 30-layers optimized structures.

Acoustic material	T, (mm)	$\boldsymbol{\rho}$, ($\mathbf{g/cm^3}$)	$\bar{\boldsymbol{\alpha}}$	$\boldsymbol{E_c}$ (MPa)	$\boldsymbol{\sigma_y}$ (MPa)	$\boldsymbol{E_c/\rho}$ (MPa $\mathbf{cm^3}$/g)	$\boldsymbol{\sigma_y/\rho}$ (MPa $\mathbf{cm^3}$/g)
1-layer (uniform microchannels)	30	0.19	0.66	524	33	2970	178
30-layers	30	0.06	0.85	82	1.3	1170	19
4-layers ($n = 6$)	30	0.05	0.84	126	1.65	2474	32
4-layers ($n = 5$)	30	0.06	0.87	201	1.9	3557	34
4-layers ($n = 4$)	30	0.07	0.86	337	6.7	4802	95
4-layers ($n = 3$)	30	0.09	0.85	468	9.0	5088	98
Melamine foam	30	0.006	0.78	0.2	0.13	33	22
Duocel® Aluminum Foam [56]	48	0.08	< 0.35	103.8	2.53	1297	32

The comparison of mechanical properties in Table 8 shows that the developed uniform microchannels and 4-layers microchannels ($n = 3$: D_2 and $D_4 = 1.00$mm) present better mechanical resistance than other 3D printed acoustic microstructures. An additional increase of the mechanical properties can be achieved using light weight and high mechanical resistant materials such as reinforced thermoplastics or thermosets.

Table 8 – Compressive mechanical properties of optimal multilayer microchannels compared to the state of the art of 3D-printed PPS

	Material	$\boldsymbol{\phi}$	$\boldsymbol{E_c}$ (MPa)	$\boldsymbol{\sigma_y}$ (MPa)
FFF optimal multilayer microchannels with 4-layers, $n = 3$	PLA	0.70	468	9.0
FFF optimal uniform microchannels	PLA	0.32	524	33
SLA TPMS uniform Schwarz P and Gyroid structures [57]	Form 2 labs white resin	0.66, 0.68	60, 41	4.0, 2.0
SLA uniform TPMS cube and gyroid [58]	PDLLA resin	0.64, 0.69	324, 169	10, 5.0
SLS TPMS Schwarz P, Schoen IWP-CM, and Neovius [59]	PA 2200 powder	0.8, 0.79, 0.78	56, 134, 150	3, 4.9, 5.6

4. Conclusions

Polymeric multilayered microchannels with increased sound absorption for different frequency ranges and high mechanical properties were developed using a comprehensive methodology including a parametric acoustic model, a numerical optimization procedure and an innovative manufacturing technique. The properties of the multilayered microchannel material were validated with acoustic and mechanical experimental characterizations. The following main results were obtained:

- Multilayered microchannels with effective acoustic properties in different frequency ranges and up to 30-layers were designed with the Nelder-Mead optimization method, the JCAL and the TMM models.
- An innovative FFF manufacturing technique was developed to produce resistive layers of microchannels with up to 100 microns and to obtain in one step multilayered structures with up to 30-layers.
- The 30mm-thick multilayered microchannels exhibit subwavelength behavior with near perfect broadband absorption in the targeted frequency ranges (absorption average up to 0.87 and NRC up to 0.46). The percentage of air of the multilayered microchannels reach up to 82% which represents a considerable economy on material, weight, and manufacturing time.
- The PLA 3D printed multilayered microchannels exhibit up to 468MPa compressive modulus and up to 9MPa compressive yield strength. Compared to other 3D printed acoustic periodic porous structures, multilayer microchannels offer a better compromise between acoustic and mechanical properties.

The importance of using a comprehensive approach accounting for the characteristics and limitations of the manufacturing method (e.g., controllable extrusion ratio and 100µm minimum perforations size) to design and obtain multilayered microchannels with increased acoustic properties was highlighted in this work. The consideration of the minimal manufacturable microchannel size during the optimization

procedure avoids the design of structures with very impressive theoretical properties that cannot be produced. The strategy of creating a specific extrusion pattern to produce minute microchannels can be used to manufacture different periodic porous structures with extrusion-based manufacturing methods. The Zigzag technique may be transposed to any other printable material including reinforced thermoplastics or epoxies which will possibly lead to structures with even higher mechanical properties. Multilayered microchannels may be produced with multinozzle techniques which can speed up the manufacturing process and may allow large scale manufacturing of multilayered microchannels. Finally, the sound absorbing material developed on this work may find applications in contexts in which noise reduction, lightweight and structural load bearing capabilities are required such as the transport industry.

Acknowledgments

The authors kindly acknowledge Safran Aircraft Engines, the Natural Sciences and Engineering Research Council of Canada (NSERC) and the doctoral training support grant program of Polytechnique Montréal (BSFD, *programme de bourses de soutien à la formation doctorale*) for supporting and funding this research. The authors also thank Jean Boulvert for providing valuable support on acoustic simulation, Kambiz Chizari for managing the reservation system and helping with the compression tests and Yanik Landry-Ducharme for cutting the sample.

Appendix A1: Complete results of optimizations with fixed l_i

A1.1. Optimization for the frequency range 500-2400Hz

Figure A1a presents the sound absorption coefficient of multilayered microchannels optimized for FR 500-2400Hz. The dashed black line corresponds to uniform microchannels (i.e. single layered). The solid lines correspond to the multilayered microchannels with 2-, 5-, 10- and 30-layers schematized in Figure A1b. Average porosity $\bar{\phi}$, frequency f_1, and absorption coefficient α_1 at the first resonant peak and the ratio of first peak wavelength to structure thickness (λ_{peak}/T) are listed in Table A1. The channel sizes of 1-, 2-, 5- and 10-layers multilayer microchannels are presented on Table A2. The first absorption peak frequency of 2-, 5-, 10- and 30-layers structures are 2080, 1665, 1500 and 1630Hz, respectively. This is 753, 1168, 1333 and 1203Hz lower than the QWRF. Multilayered microchannels are lighter and present better absorption capabilities than uniform microchannels.

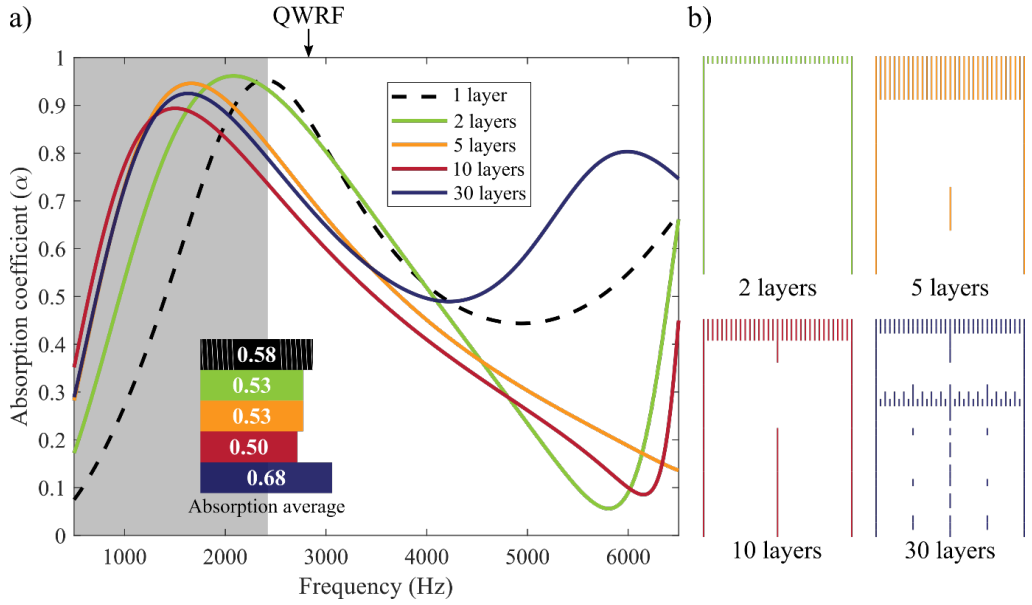

Figure A1 – Results of optimization for the frequency range 500-2400Hz: (a) Comparison of the absorption coefficient of the multilayer and uniform microchannels (b) Scheme of the resulting multilayer configurations.

Table A1 – $\bar{\phi}$, f_1, α_1 and λ_{peak}/L of structures optimized for the frequency range 500-2400Hz

Configuration	Percentage of air, $\bar{\phi}$ (%)	Frequency at first peak (f_1)	Absorption at first peak (α_1)	Ratio first peak wavelength to structure thickness (λ_{peak}/T)
1-layer	30	2392Hz	0.95	4.7
2-layers	93	2080Hz	0.96	5.4
5-layers	81	1660Hz	0.94	6.8
10-layers	85	1504Hz	0.89	7.5
30-layers	82	1631Hz	0.92	6.9

Table A2 – Channel sizes of the 1-, 2-, 5- and 10-layers optimized structures for frequency range 500-2400Hz

	1-layer	2-layers	5-layers	10-layers

D_1	0.24mm	0.10mm	0.16mm	0.10mm
D_2	-	9.40mm	11.32mm	4.60mm
D_3		-	11.32mm	9.40mm
D_4			5.56mm	9.40mm
D_5			11.32mm	9.40mm
D_6			-	4.60mm
D_7				4.60mm
D_8				4.60mm
D_9				4.60mm
D_{10}				4.60mm

A1.2. Optimization for the frequency range 2400-6500Hz

Figure A2 presents the sound absorption coefficient of structures optimized for FR 2400-6500Hz. Figure A2 presents a 2D schematic of the multilayered microchannels. $\bar{\phi}$, f_1, α_1 and λ_{peak}/T are listed o n Table A3. The channels size of 1-, 2-, 5- and 10-layers structures are presented on Table A4. The 30-layers structure presents the broader absorption spectrum and the higher absorption average ($\bar{\alpha} = 0.82$). This is 41% higher than the uniform microchannels, 5% higher than the 5-layers and 3% higher than the 10-layers multilayered microchannels. Additionally, the 30-layers structure present the higher percentage of air ($\bar{\phi}$ = 73%).

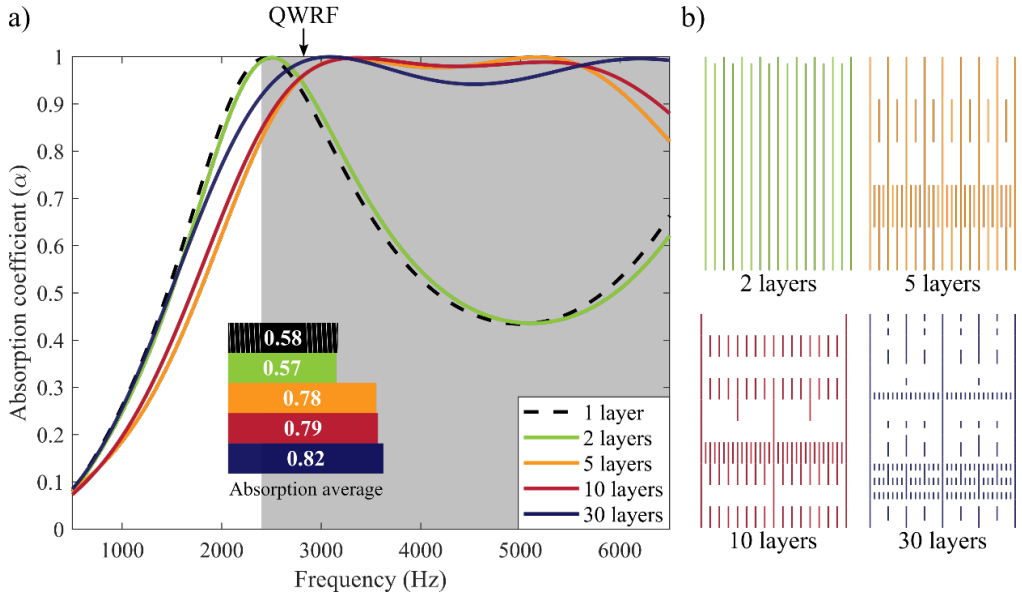

Figure A2 – Results of optimization for the frequency range 2400-6500Hz: (a) Comparison of the absorption coefficient of the multilayer and uniform microchannels (b) Scheme of the resulting multilayer configurations.

Table A3 – $\bar{\phi}$, f_1, α_1 and λ_{peak}/L of structures with optimized absorption for frequency range 2400-6500Hz

Configuration	Percentage of air, $\bar{\phi}$ (%)	Frequency at first peak (f_1)	Absorption at first peak (α_1)	Ratio first peak wavelength to structure thickness (λ_{peak}/T)
1-layer	34	2450Hz	1.0	4.6
2-layers	35	2505Hz	1.0	4.5

5-layers	49	3288Hz	1.0	3.4
10-layers	67	3355Hz	1.0	3.4
30-layers	73	3085Hz	1.0	3.7

Table A4 – Channels size of the 1-, 2-, 5- and 10-layers optimized structures for frequency range 2400-6500Hz

	1-layer	2-layers	5-layers	10-layers
D_1	0.28mm	0.76mm	1.16mm	10.04mm
D_2	-	0.28mm	0.48mm	0.44mm
D_3		-	1.16mm	10.04mm
D_4			0.14mm	0.44mm
D_5			0.48mm	2.36mm
D_6			-	4.92mm
D_7				0.12mm
D_8				0.44mm
D_9				4.92mm
D_{10}				0.44mm

A1.3. Optimization for the frequency range 500-6500Hz

Figure A3a presents the sound absorption coefficient of structures optimized for FR 500-6500Hz. Figure A3b presents a 2D schematic of the multilayered microchannels. $\bar{\phi}$, f_1, α_1 and λ_{peak}/T are listed in Table A5. The channels size of 1-, 2-, 5- and 10-layers structures are presented on Table A6. The 30-layers structure presents the highest absorption average of all multilayered structures, $\bar{\alpha} = 0.86$. The 30-layers structure exhibits also subwavelength behavior ($\lambda_{peak}/T = 5.5$) and broadband acoustic absorption with the first peak located at 2075Hz.

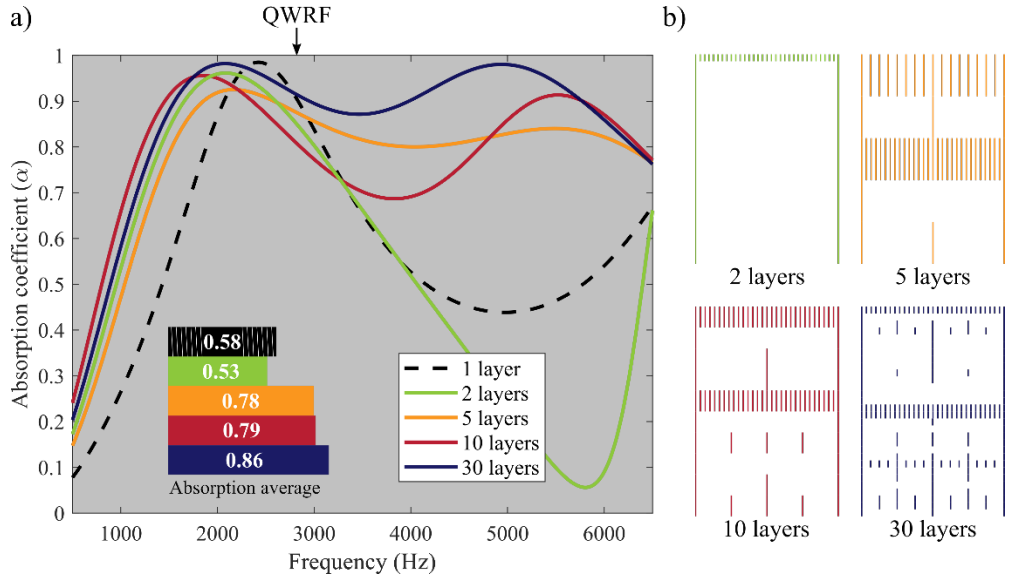

Figure A3 – Optimization results for the frequency range 500-6500Hz: (a) Comparison of the absorption coefficient of the multilayer and uniform microchannels (b) Scheme of the resulting multilayer configurations.

Table A5 – $\bar{\phi}$, f_1, α_1 and λ_{peak}/L of structures with optimized absorption for frequency range 6500Hz

Configuration	Percentage of air, $\bar{\phi}$ (%)	Frequency at first peak (f_1)	Absorption at first peak (α_1)	Ratio wavelength at first peak to structure thickness (λ_{peak}/T)
1-layer	32	2420Hz	0.98	4.7
2-layers	93	2080Hz	0.96	5.4
5-layers	70	2165Hz	0.92	5.2
10-layers	78	1850Hz	0.96	6.1
30-layers	79	2075Hz	0.98	5.5

Table A6 – Channels size of the 1-, 2-, 5- and 10-layers optimized structure 500-6500Hz

	1-layer	2-layers	5-layers	10-layers
D_1	0.26mm	0.10mm	0.48mm	0.16mm
D_2	-	9.40mm	5.24mm	11.32mm
D_3		-	0.14mm	5.56mm
D_4			10.68mm	5.56mm
D_5			5.24mm	0.16mm
D_6			-	11.32mm
D_7				2.68mm
D_8				11.32mm
D_9				5.56mm
D_{10}				2.68mm

Appendix A2: Supplementary results for 500-6500Hz frequency range

Additional optimizations were performed to further investigate the best possible configurations for sound absorption on the FR 500-6500Hz. The optimizations were done with all parameters free to vary (i.e., variable number of layers, N layer thickness, l_i and channels size D_i) and with variable l_i and D_i for specific numbers of layers, namely N = 4-, 6-, 10- and 30. 10000 iterations were used for the former and 2000 for the latter to increase the probability to find the global minimum. The absorption curves and schemes of the resulting multilayered structures are shown on Figure A**4**a and b, respectively. The thickness of the multilayered structures is 30mm. The curve for the 30-layers structure optimized with fixed l_i = 1mm is also plotted for comparation purpose. Table A7 lists the cost function, J, the difference of J relative to the 30 layers fixed l_i = 1mm, the absorption average, $\bar{\alpha}$, and the percentage of air, $\bar{\phi}$ of the resulting configurations. The absorption curves are very similar. The maximum absorption average is 0.86 and the minimum is 0.83. All absorption curves show two absorption peaks. The first peak is located approximately at the same frequency (around 2000Hz) for all configurations, and the absorption coefficient at the peak does not deviate more than 0.1. The main difference appears on the position and the level of the 2nd absorption peak and the position and thickness of the 2nd resistive layer. The 2nd absorption peak of the 6- and 10-layers structures is ~500Hz lower in frequency. This characteristic seems to be related to the increased thickness and the lower position on the z axis of the 2nd resistive layer. All absorption curves further indicate that for better absorption on the FR 500-6500Hz the best solution is a 2 degree of freedom structure. The number of layers found on the optimization with variable N is 23 (pink curve and structure). The best solution is the 4-layers structure. The cost function of the 4-layers structure is 14.28 which is 3.38% lower than the 30-layers structure optimized with fixed l_i = 1mm. Besides presenting the best final cost function, the 4-layers structures are simpler and therefore easier to manufacture than the 5-, 6-, 10- or 30-layers configurations.

Table A7 – Cost function, J the percentage difference of the cost functions compared to the optimized 30-layers with fixed l_i = 1mm, the absorption average, $\bar{\boldsymbol{\alpha}}$ and the percentage of air, $\bar{\boldsymbol{\phi}}$

Configuration	Cost function, J	Difference of J relative to the 30 layers fixed l_i = 1mm (%)	Absorption average, $\bar{\boldsymbol{\alpha}}$	Percentage of air, $\bar{\boldsymbol{\phi}}$ (%)
30 layers fixed l_i = 1mm	14.79	-	0.86	79
Variable N, D_i and l_i	14.48	-2.09	0.86	80
4-layers variable l_i	14.29	- 3.38	0.85	83
6-layers variable l_i	15.50	+ 4.80	0.83	73
10-layers variable l_i	14.67	- 0.81	0.86	79
30-layers variable l_i	14.88	+ 0.61	0.86	81

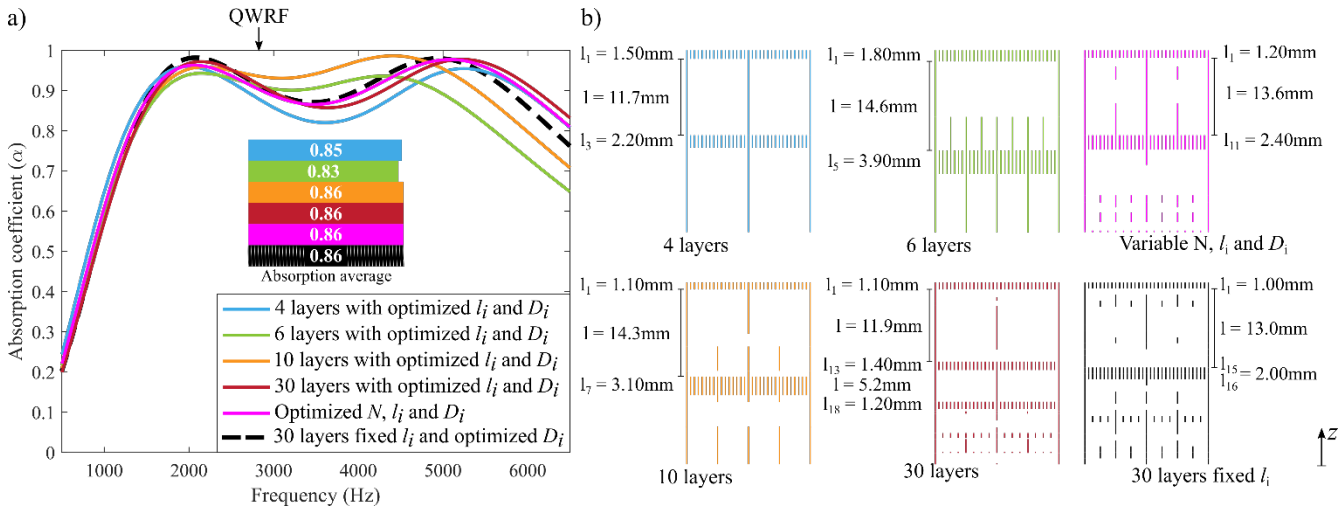

Figure A4 – Multilayered microchannels optimized for the frequency range 500-6500Hz. (a) Comparison of the absorption coefficient (b) Scheme of the resulting multilayer configurations.

Appendix A3: Simulations of different 4-layers structures

Figure A5 shows the simulated sound absorption coefficient and the schemes of the multilayered structures (30- and 4-layers). Table A8 lists $\bar{\alpha}$ and $\bar{\phi}$ of the configurations. The 4-layers structures with n = 6 and 5 show the best sound absorption average ($\bar{\alpha}$ = 0.87). Compared to the 30-layers structure optimized for fixed l_i = 1mm, the 4-layers structures with n = 6 is slightly better because of the larger channels of the permeable layers. However, with D_2 and D_4 = 4.60mm and 9.40mm these structures present poor mechanical properties. Compared to the best 4-layers structures (n = 6), a decrease of 1, 2 and 10% of the absorption average is observed for the 4-layers structures with n = 4, 3 and 2, respectively. From a practical point of view, the sound absorption of the 4-layers structures with n = 6, 5 and 4 are virtually equivalent indicating that their absorption is independent of the channels size of the permeable layers because most of the viscous and thermal losses occur in the resistive layers. Therefore, a good compromise between mechanical and acoustic properties may be found.

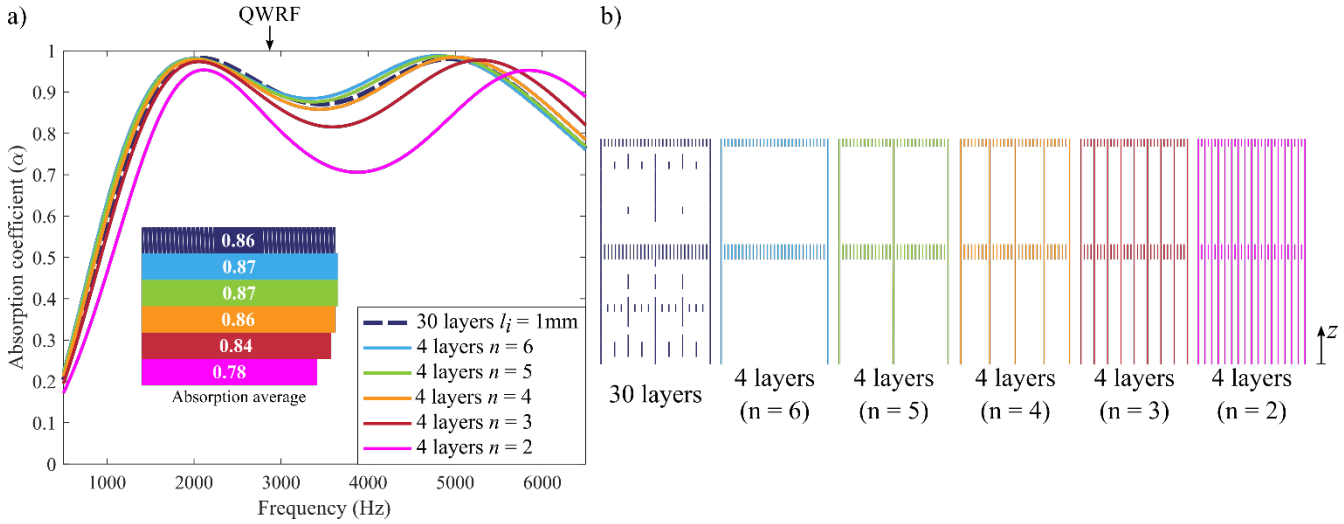

Figure A5 - Multilayered microchannels with different permeable layers channels size (a) comparison of the absorption coefficient of the multilayer structures (b) Scheme of the multilayer configurations.

Table A8 - The absorption average, $\bar{\alpha}$ and the average of the porosity, $\bar{\phi}$ of configurations with different permeable channels size

Configuration	Absorption average, $\bar{\alpha}$	Percentage of air, $\bar{\phi}$ (%)
30-layers fixed l_i = 1mm	0.86	79
4-layers n = 6	0.87	87
4-layers n = 5	0.87	84
4-layers n = 4	0.86	77
4-layers n = 3	0.84	64
4-layers n = 2	0.78	42

REFERENCES

[1] E.R. Fotsing, A. Dubourg, A. Ross, J. Mardjono, Acoustic properties of periodic micro-structures obtained by additive manufacturing, Appl. Acoust. 148 (2019) 322–331. https://doi.org/10.1016/j.apacoust.2018.12.030.

[2] J. Boulvert, J. Costa-Baptista, T. Cavalieri, M. Perna, E.R. Fotsing, V. Romero-García, G. Gabard, A. Ross, J. Mardjono, J.-P. Groby, Acoustic modeling of micro-lattices obtained by additive manufacturing, Appl. Acoust. 164 (2020) 107244. https://doi.org/10.1016/j.apacoust.2020.107244.

[3] X. Cai, J. Yang, G. Hu, T. Lu, Sound absorption by acoustic microlattice with optimized pore configuration, J. Acoust. Soc. Am. 144 (2018) EL138–EL143. https://doi.org/10.1121/1.5051526.

[4] J. Costa-Baptista, E.-R. Fotsing, J. Boulvert, J. Mardjono, D. Therriault, A. Ross, Sonic crystal acoustic absorbers produced by fugitive ink, in: 1st Aerosp. Eur. Conf., Bordeaux, 2020: p. 8.

[5] D.D. C Jiang, D Moreau, Acoustic Absorption of Porous Materials Produced by Additive Manufacturing with Varying Geometries, in: Proc. Acoust. 2017, 2017. https://www.acoustics.asn.au/conference_proceedings/AAS2017/papers/p79.pdf.

[6] D.C. Akiwate, M.D. Date, B. Venkatesham, S. Suryakumar, Acoustic properties of additive manufactured narrow tube periodic structures, Appl. Acoust. 136 (2018) 123–131. https://doi.org/10.1016/j.apacoust.2018.02.022.

[7] Z. Liu, J. Zhan, M. Fard, J.L. Davy, Acoustic properties of a porous polycarbonate material produced by additive manufacturing, Mater. Lett. 181 (2016) 296–299. https://doi.org/10.1016/j.matlet.2016.06.045.

[8] W. Johnston, B. Sharma, Additive manufacturing of fibrous sound absorbers, Addit. Manuf. 41 (2021) 101984. https://doi.org/10.1016/j.addma.2021.101984.

[9] N. Gao, H. Hou, Sound absorption characteristic of micro-helix metamaterial by 3D printing, Theor. Appl. Mech. Lett. 8 (2018) 63–67. https://doi.org/10.1016/j.taml.2018.02.001.

[10] K. Monkova, M. Vasina, P.P. Monka, D. Kozak, J. Vanca, Effect of the pore shape and size of 3d-printed open-porous abs materials on sound absorption performance, Materials (Basel). 13 (2020) 1–19. https://doi.org/10.3390/ma13204474.

[11] W. Yang, J. An, C.K. Chua, K. Zhou, Acoustic absorptions of multifunctional polymeric cellular structures based on triply periodic minimal surfaces fabricated by stereolithography, Virtual Phys. Prototyp. 15 (2020) 242–249. https://doi.org/10.1080/17452759.2020.1740747.

[12] H.J. Rice, J. Kennedy, P. Göransson, L. Dowling, D. Trimble, Design of a Kelvin cell acoustic metamaterial, J. Sound Vib. 472 (2020) 115167. https://doi.org/10.1016/j.jsv.2019.115167.

[13] S. Deshmukh, H. Ronge, S. Ramamoorthy, Design of periodic foam structures for acoustic applications: Concept, parametric study and experimental validation, Mater. Des. 175 (2019) 107830. https://doi.org/10.1016/j.matdes.2019.107830.

[14] J. Kennedy, L. Flanagan, L. Dowling, G.J. Bennett, H. Rice, D. Trimble, The Influence of Additive Manufacturing Processes on the Performance of a Periodic Acoustic Metamaterial, Int. J. Polym. Sci. 2019 (2019) 1–11. https://doi.org/10.1155/2019/7029143.

[15] T.G. Zieliński, K.C. Opiela, P. Pawłowski, N. Dauchez, T. Boutin, J. Kennedy, D. Trimble, H. Rice, B. Van Damme, G. Hannema, R. Wróbel, S. Kim, S. Ghaffari Mosanenzadeh, N.X. Fang, J. Yang, B. Briere de La Hosseraye, M.C.J. Hornikx, E. Salze, M.-A. Galland, R. Boonen, A. Carvalho de Sousa, E. Deckers, M. Gaborit, J.-P. Groby, Reproducibility of sound-absorbing periodic porous materials using additive manufacturing technologies: Round robin study, Addit. Manuf. 36 (2020) 101564. https://doi.org/10.1016/j.addma.2020.101564.

[16] X. Olny, C. Boutin, Acoustic wave propagation in double porosity media, J. Acoust. Soc. Am. 114 (2003) 73–89. https://doi.org/10.1121/1.1534607.

[17] R. Venegas, O. Umnova, Acoustical properties of double porosity granular materials, J. Acoust.

Soc. Am. 130 (2011) 2765–2776. https://doi.org/10.1121/1.3644915.
[18] H. Zhao, Y. Wang, D. Yu, H. Yang, J. Zhong, F. Wu, J. Wen, A double porosity material for low frequency sound absorption, Compos. Struct. 239 (2020) 111978. https://doi.org/10.1016/j.compstruct.2020.111978.
[19] J.S. Lee, E. Il Kim, Y.Y. Kim, J.S. Kim, Y.J. Kang, Optimal poroelastic layer sequencing for sound transmission loss maximization by topology optimization method, J. Acoust. Soc. Am. 122 (2007) 2097–2106. https://doi.org/10.1121/1.2770541.
[20] H. Pichon, E. Piollet, A. Ross, An acoustic trade-off chart for the design of multilayer acoustic packages, Appl. Acoust. 148 (2019) 9–18. https://doi.org/10.1016/j.apacoust.2018.12.003.
[21] C. Lagarrigue, J.P. Groby, V. Tournat, O. Dazel, O. Umnova, Absorption of sound by porous layers with embedded periodic arrays of resonant inclusions, J. Acoust. Soc. Am. 134 (2013) 4670–4680. https://doi.org/10.1121/1.4824843.
[22] O. Doutres, N. Atalla, H. Osman, Modeling and experimental validation of cellular porous material with large resonant inclusions, INTERNOISE 2014 - 43rd Int. Congr. Noise Control Eng. Improv. World Through Noise Control. 137 (2014) 3502–3513.
[23] J.-P. Groby, C. Lagarrigue, B. Brouard, O. Dazel, V. Tournat, B. Nennig, Using simple shape three-dimensional rigid inclusions to enhance porous layer absorption, J. Acoust. Soc. Am. 136 (2014) 1139–1148. https://doi.org/10.1121/1.4892760.
[24] Yang, Bai, Zhu, Kiran, An, Chua, Zhou, 3D Printing of Polymeric Multi-Layer Micro-Perforated Panels for Tunable Wideband Sound Absorption, Polymers (Basel). 12 (2020) 360. https://doi.org/10.3390/polym12020360.
[25] D.C. Akiwate, M.D. Date, B. Venkatesham, S. Suryakumar, Acoustic characterization of additive manufactured perforated panel backed by honeycomb structure with circular and non-circular perforations, Appl. Acoust. 155 (2019) 271–279. https://doi.org/10.1016/j.apacoust.2019.05.025.
[26] J. Carbajo, S. Ghaffari Mosanenzadeh, S. Kim, N.X. Fang, Multi-layer perforated panel absorbers with oblique perforations, Appl. Acoust. 169 (2020) 107496. https://doi.org/10.1016/j.apacoust.2020.107496.
[27] D.-Y. Maa, Potential of microperforated panel absorber, J. Acoust. Soc. Am. 104 (1998) 2861–2866. https://doi.org/10.1121/1.423870.
[28] Y.J. Qian, D.Y. Kong, S.M. Liu, S.M. Sun, Z. Zhao, Investigation on micro-perforated panel absorber with ultra-micro perforations, Appl. Acoust. 74 (2013) 931–935. https://doi.org/10.1016/j.apacoust.2013.01.009.
[29] Y. Tang, F. Xin, T.J. Lu, Sound absorption of micro-perforated sandwich panel with honeycomb-corrugation hybrid core at high temperatures, Compos. Struct. 226 (2019) 111285. https://doi.org/10.1016/j.compstruct.2019.111285.
[30] J. Boulvert, T. Cavalieri, J. Costa-Baptista, L. Schwan, V. Romero-García, G. Gabard, E.R. Fotsing, A. Ross, J. Mardjono, J.-P. Groby, Optimally graded porous material for broadband perfect absorption of sound, J. Appl. Phys. 126 (2019) 175101. https://doi.org/10.1063/1.5119715.
[31] T. Cavalieri, J. Boulvert, G. Gabard, V. Romero-García, M. Escouflaire, J. Regnard, J.-P. Groby, Graded and Anisotropic Porous Materials for Broadband and Angular Maximal Acoustic Absorption, Materials (Basel). 13 (2020) 4605. https://doi.org/10.3390/ma13204605.
[32] J.C. Baptista, E. Roland-Fotsing, J. Mardjano, D. Therriault, A. Ross, Multilayer treatment for subwavelength and broadband absorption, in: INTER-NOISE NOISE-CON Congr. Conf. Proc., Institute of Noise Control Engineering, 2021: pp. 2219–2227.
[33] A. Dubourg, Intégration de structures absorbantes acoustique innovantes au sein d'une turbosouffante, (2015) 142. https://publications.polymtl.ca/2045/.
[34] D.L. Johnson, J. Koplik, R. Dashen, Theory of dynamic permeability and tortuosity in fluid-saturated porous media, J. Fluid Mech. 176 (1987) 379. https://doi.org/10.1017/S0022112087000727.

[35] Y. Champoux, J. Allard, Dynamic tortuosity and bulk modulus in air-saturated porous media, J. Appl. Phys. 70 (1991) 1975–1979. https://doi.org/10.1063/1.349482.
[36] D. Lafarge, P. Lemarinier, J.F. Allard, V. Tarnow, Dynamic compressibility of air in porous structures at audible frequencies, J. Acoust. Soc. Am. 102 (1997) 1995–2006. https://doi.org/10.1121/1.419690.
[37] J.F. Allard, N. Atalla, Propagation of Sound in Porous Media: Modelling Sound Absorbing Materials, 2nd ed., John Wiley & Sons, Ltd, Chichester, UK, 2009. https://doi.org/10.1002/9780470747339.
[38] N. Atalla, F. Sgard, Modeling of perforated plates and screens using rigid frame porous models, J. Sound Vib. 303 (2007) 195–208. https://doi.org/10.1016/j.jsv.2007.01.012.
[39] R. Panneton, X. Olny, Acoustical determination of the parameters governing viscous dissipation in porous media, J. Acoust. Soc. Am. 119 (2006) 2027–2040. https://doi.org/10.1121/1.2169923.
[40] X. Olny, R. Panneton, Acoustical determination of the parameters governing thermal dissipation in porous media, J. Acoust. Soc. Am. 123 (2008) 814–824. https://doi.org/10.1121/1.2828066.
[41] Luc Jaouen, APMR : Acoustical Porous Material Recipes, Matelys. (2022). https://apmr.matelys.com/ (accessed December 19, 2021).
[42] J.-L. Auriault, C. Boutin, C. Geindreau, Homogenization of Coupled Phenomena in Heterogenous Media, ISTE, London, UK, 2009. https://doi.org/10.1002/9780470612033.
[43] T.G. Zieliński, R. Venegas, C. Perrot, M. Červenka, F. Chevillotte, K. Attenborough, Benchmarks for microstructure-based modelling of sound absorbing rigid-frame porous media, J. Sound Vib. 483 (2020) 115441. https://doi.org/10.1016/j.jsv.2020.115441.
[44] J. D'Errico, Bound constrained optimization using fminsearch, MATLAB Cent. File Exch. (2010). http://www.mathworks.com/matlabcentral/fileexchange/8277-fminsearchbnd.
[45] L. Lei, N. Dauchez, J.D. Chazot, Prediction of the six parameters of an equivalent fluid model for thermocompressed glass wools and melamine foam, Appl. Acoust. 139 (2018) 44–56. https://doi.org/10.1016/j.apacoust.2018.04.010.
[46] ASTM International, ASTM E1050−12: Standard Test Method for Impedance and Absorption of Acoustical Materials Using a Tube, Two Microphones and a Digital Frequency Analysis System, (2012). https://doi.org/https://doi.org/10.1520/D0695-15.
[47] ISO, 10534–2: Acoustics—Determination of Sound Absorption Coefficient and Impedance in Impedance Tubes—Part 2: Transfer-Function Method., 1998.
[48] ASTM, ASTM D695 - 15: Standard Test Method for Compressive Properties of Rigid Plastics, in: US, 2015: p. 8. https://doi.org/10.1520/D0695-15.
[49] H. Ruiz, P. Cobo, T. Dupont, B. Martin, P. Leclaire, Acoustic properties of plates with unevenly distributed macroperforations backed by woven meshes, J. Acoust. Soc. Am. 132 (2012) 3138–3147. https://doi.org/10.1121/1.4754520.
[50] J. Costa-Baptista, E.R. Fotsing, J. Boulvert, J. Mardjono, D. Therriault, A. Ross, Design and fused filament fabrication of microchannels with high broadband sound absorption, Appl. Acoust. (2022) Under review.
[51] D. Brzeski, I.L. Hia, J.-F. Chauvette, R.D. Farahani, N. Piccirelli, A. Ross, D. Therriault, Design of thermoset composites for high-speed additive manufacturing of lightweight sound absorbing micro-scaffolds, Addit. Manuf. 47 (2021) 102245. https://doi.org/10.1016/j.addma.2021.102245.
[52] J.-F. Chauvette, D. Brzeski, I.L. Hia, R.D. Farahani, N. Piccirelli, D. Therriault, High-speed multinozzle additive manufacturing and extrusion modeling of large-scale microscaffold networks, Addit. Manuf. 47 (2021) 102294. https://doi.org/10.1016/j.addma.2021.102294.
[53] Z. Xu, W. He, F. Xin, T.J. Lu, Sound propagation in porous materials containing rough tubes, Phys. Fluids. 32 (2020) 093604. https://doi.org/10.1063/5.0017710.
[54] J.C.S. McCaw, E. Cuan-Urquizo, Mechanical characterization of 3D printed, non-planar lattice structures under quasi-static cyclic loading, Rapid Prototyp. J. 26 (2020) 707–717.

https://doi.org/10.1108/RPJ-06-2019-0163.
[55] B. Brenken, E. Barocio, A. Favaloro, V. Kunc, R.B. Pipes, Fused filament fabrication of fiber-reinforced polymers: A review, Addit. Manuf. 21 (2018) 1–16. https://doi.org/10.1016/j.addma.2018.01.002.
[56] M.J. Cops, J.G. McDaniel, E.A. Magliula, D.J. Bamford, J. Bliefnick, Measurement and analysis of sound absorption by a composite foam, Appl. Acoust. 160 (2020) 107138. https://doi.org/10.1016/j.apacoust.2019.107138.
[57] S. Yu, J. Sun, J. Bai, Investigation of functionally graded TPMS structures fabricated by additive manufacturing, Mater. Des. 182 (2019) 108021. https://doi.org/10.1016/j.matdes.2019.108021.
[58] F.P.W. Melchels, K. Bertoldi, R. Gabbrielli, A.H. Velders, J. Feijen, D.W. Grijpma, Mathematically defined tissue engineering scaffold architectures prepared by stereolithography, Biomaterials. 31 (2010) 6909–6916. https://doi.org/10.1016/j.biomaterials.2010.05.068.
[59] D.W. Abueidda, M. Bakir, R.K. Abu Al-Rub, J.S. Bergström, N.A. Sobh, I. Jasiuk, Mechanical properties of 3D printed polymeric cellular materials with triply periodic minimal surface architectures, Mater. Des. 122 (2017) 255–267. https://doi.org/10.1016/j.matdes.2017.03.018.